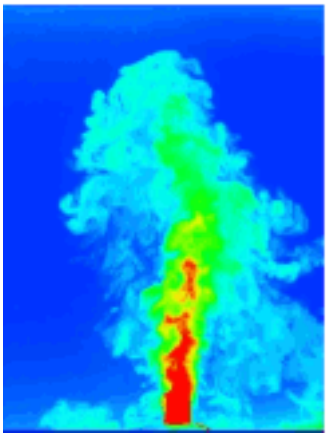

Journal of Turbulence
Publication details, including instructions for authors and subscription information:
http://www.tandfonline.com/loi/tjot20

A Reynolds stress model for turbulent flows of viscoelastic fluids

P.R. Resende[a], F.T. Pinho[b] & D.O. Cruz[c]

[a] Grupo de Automação e Sistemas Integráveis, UNESP - Universidade Estadual Paulista, Sorocaba, Brazil

[b] Departamento de Engenharia Mecânica, Centro de Estudos de Fenómenos de Transporte, Faculdade de Engenharia Universidade do Porto, Porto, Portugal

[c] Programa de Engenharia Mecânica (DEM/COPPE/UFRJ), Rio de Janeiro, Brazil

Published online: 10 Dec 2013.

To cite this article: P.R. Resende, F.T. Pinho & D.O. Cruz (2013) A Reynolds stress model for turbulent flows of viscoelastic fluids, Journal of Turbulence, 14:12, 1-36

To link to this article: http://dx.doi.org/10.1080/14685248.2013.851385

Journal of Turbulence, 2013
Vol. 14, No. 12, 1–36, http://dx.doi.org/10.1080/14685248.2013.851385

A Reynolds stress model for turbulent flows of viscoelastic fluids

P.R. Resende[a*], F.T. Pinho[b] and D.O. Cruz[c]

[a]*Grupo de Automação e Sistemas Integráveis, UNESP – Universidade Estadual Paulista, Sorocaba, Brazil;* [b]*Departamento de Engenharia Mecânica, Centro de Estudos de Fenómenos de Transporte, Faculdade de Engenharia Universidade do Porto, Porto, Portugal;* [c]*Programa de Engenharia Mecânica (DEM/COPPE/UFRJ), Rio de Janeiro, Brazil*

(*Received 29 May 2013; accepted 26 September 2013*)

A second-order closure is developed for predicting turbulent flows of viscoelastic fluids described by a modified generalised Newtonian fluid model incorporating a nonlinear viscosity that depends on a strain-hardening Trouton ratio as a means to handle some of the effects of viscoelasticity upon turbulent flows. Its performance is assessed by comparing its predictions for fully developed turbulent pipe flow with experimental data for four different dilute polymeric solutions and also with two sets of direct numerical simulation data for fluids theoretically described by the finitely extensible nonlinear elastic – Peterlin model. The model is based on a Newtonian Reynolds stress closure to predict Newtonian fluid flows, which incorporates low Reynolds number damping functions to properly deal with wall effects and to provide the capability to handle fluid viscoelasticity more effectively. This new turbulence model was able to capture well the drag reduction of various viscoelastic fluids over a wide range of Reynolds numbers and performed better than previously developed models for the same type of constitutive equation, even if the streamwise and wall-normal turbulence intensities were underpredicted.

Keywords: turbulence model; drag reduction; polymer solutions; second-order closure

1. Introduction

The first turbulence models for viscoelastic fluid flows date from the 1970s with [1–3] and were both motivated and aimed at drag reduction by polymer solutions in turbulent pipe and channel flows. The scope of these earlier models was rather limited, because they depended to a large extent on parameters that needed to be selected for each fluid in each flow situation and were just modifications of turbulence models for Newtonian fluids. These models had no link between the flow dynamics and the non-Newtonian rheology, with the exception of Mizushina et al.'s [1] model, which incorporated effects of relaxation time in the Van Driest damping function for the eddy viscosity. In the 1980s and 1990s, new two-equation turbulence models appeared [4–6], this time linking the model development with fluid rheology, but these models were limited to inelastic fluids described by the power law viscosity model, where the viscosity function depends on the second invariant of the rate of deformation tensor.

The development of turbulence models based on rheological constitutive equations for viscoelastic fluids has taken place this century along two different but complementary paths. One method, embodied in the works of [7–10] and the present contribution, relies

*Corresponding author. Email: resende@sorocaba.unesp.br

on the adoption of a generalised Newtonian fluid (GNF) constitutive equation that models some relevant behaviour of real polymer solutions. The GNF model has been modified to incorporate the effect of elastic properties that are known to be relevant in the context of turbulent flows of drag-reducing viscoelastic fluids. This is accomplished by incorporating simultaneously the dependence of the viscosity on the second and third invariants of the instantaneous rate of deformation tensor, the latter via an indexer of the Trouton ratio. This constitutive model does not possess memory effects, but does incorporate strain hardening, which here has been made to act directly into the viscosity function. In these works, experimental data were used for both the fluid rheology and the flow dynamics for the purpose of calibration and validation of the turbulence models, which are capable of predicting the experimentally measured flow characteristics in fully developed pipe flow.

The second approach to turbulence modelling of viscoelastic fluid flows is more fundamental, but in contrast to the previous approach, it has not yet been able to reproduce experimental data quantitatively. Here, the development of the turbulence closures and their calibration and validation rely on post-processed direct numerical simulation (DNS) data for viscoelastic constitutive equations, which only agree qualitatively with experimental data. Even though there are DNS data-sets for several models such as the finitely extensible nonlinear elastic model with Peterlin's closure (FENE-P), the Oldroyd-B model [11] and the Giesekus constitutive equation [12,13], the development of Reynolds-averaged Navier–Stokes (RANS) models has been restricted to fluids described by the FENE-P constitutive equation and the existing discrepancies relative to experimental data [14] have so far been attributed to the inherent simplicity of the underlying dumb-bell model, such as the lack of configurational degrees of freedom, the oversimplification of the Peterlin closure of the FENE equation [15], whose failure is even more dramatic in the context of turbulent flow [16] and to concentration and polymer degradation effects in experiments, amongst others.

Using the DNS data for FENE-P fluids, several turbulence models have been developed, such as the eddy viscosity closure of Li et al. [17], the k–ε models of Pinho and co-workers [18,19], the k–ω model of Resende et al. [20] and the k–ε–v^2–f closures of the Stanford group [21,22]. Regarding the two most recent models of this set, the adoption of Durbin's approach [23] for the eddy viscosity by Iaccarino et al. [22] is particularly successful at predicting the whole range of drag reduction for the FENE-P fluids, but is unable to predict all components of the polymer stress in turbulent flow, in contrast to the model of Resende et al. [19] which can predict all components of the polymer stress tensor. However, the model of Resende et al. [19] has a poorer prediction of the Reynolds stresses and its range of application is limited to about 50% drag reduction, since it invokes turbulence isotropy.

Therefore, in spite of their promise, rooted on apparently a more realistic constitutive equation, none of these models for FENE-P fluids is yet capable of predicting quantitatively experimental flows and this is unrelated to limitations of the turbulent closures, in contrast to the predictions by the turbulence model relying on the simpler modified generalised Newtonian model, which have always been developed against experimental data. In fact, for the reasons invoked above, experiments with polymer solutions and DNS performed on a FENE-P model with parameters quantified by the corresponding rheological and flow rate measurements give results with a significant disagreement in regard to the amount of drag reduction and consequently of the various stress profiles [14], so it is not surprising that the corresponding turbulence models also fail to quantitatively predict such flows.

Summarising, on one side there are turbulence models grounded on simpler constitutive equations, which are capable of predicting experimental flows, and on the other side there are turbulence models rooted on more robust viscoelastic rheological equations, but which fail to predict quantitatively experimental flows, thus showing that a lot of ground still

needs to be threaded. Thus, the reason for developing a second-order turbulence model for the modified GNF constitutive equation is clear: to improve on existing turbulence models for the modified GNF equation that are able to predict real flows of viscoelastic polymer solutions, but which were also developed on the basis of isotropic turbulence. Additionally, and in spite of the different rheological constitutive equations upon which the two families of turbulence models are based on, they share common features and predictive capabilities, so that the earlier k–ε models of Pinho and co-workers [9,10] for GNF fluids largely facilitated their development of the k–ε model for the FENE-P fluids [18,19], and similarly, we expect the development of this second-order turbulence closure to facilitate the future development of a second-order model for FENE-P fluids. In this respect, modifications will need to be implemented in the future on the viscoelastic constitutive equations, such as the FENE-P model, in order to allow them to predict experimental turbulent flows via a new generation of turbulence models. The existing turbulence closures for viscoelastic fluids represented by both the modified GNF and the FENE-P constitutive equations will help to arrive at a compromise between prediction accuracy by a complex theoretical model and the capacity to solve real engineering problems using a simpler constitutive equation as an alternative to start all over again with a different and better, but certainly more complex viscoelastic constitutive equation.

In the remainder of this introduction, we briefly explain the development of the existing two equation models for the modified GNF rheological constitutive equation followed by an overview of second-order turbulence models for Newtonian fluids in order to understand the selection of the base model and the scope of the present contribution.

The original first-order turbulence model developed following this approach is described in detail in [7,8] by Pinho [7] and Cruz and Pinho [8]. This is a low Reynolds number k–ε model, which was developed on the basis of the Nagano and Hishida's k–ε model [24] for Newtonian fluids, and includes a closure for the Reynolds-averaged molecular viscosity, in order to properly account for the effect of fluctuating strain rates on the nonlinear viscosity function, and a damping function for the eddy viscosity to account for wall proximity, shear thinning of the shear viscosity and strain thickening of the Trouton ratio. However, this turbulence model neglected the new term of the momentum equation quantifying the cross correlation between the fluctuating viscosity and the fluctuating rate of deformation, which was called pseudo-elastic stress and for which a closure was subsequently developed by Cruz et al. [9]. They also accounted for and developed the closure for the extra stress work term originating from the pseudo-elastic stress appearing in the transport equation of turbulent kinetic energy. Consideration of this pseudo-elastic stress work improved the predictions of turbulent kinetic energy and of friction factors especially at large Reynolds numbers.

Duct flows with drag reduction have enhanced anisotropy of the Reynolds stresses as shown in experimental work [10,14,25] and in DNS investigations with various differential viscoelastic models [11,12,26]. However, turbulence anisotropy is not captured by linear forms of the k–ε turbulence model and requires either the use of higher order versions of the eddy viscosity closure as was done by Resende et al. [10] using a nonlinear k–ε model or higher order turbulence models as is done in this work. This latter option brings additional benefits to complex flow prediction such as a more realistic description of turbulence by the use of transport equations for the individual Reynolds stresses, which incorporates, amongst other things such effects as the pressure-strain mechanism for the distribution of turbulent kinetic energy components or a better capability to deal with flows with curvature. In fact, first-order turbulence models have shortcomings when it comes to predicting Newtonian flows with separation or streamline curvature, amongst other things (cf. [27]).

The use of anisotropic first-order models can offset some, but not all, of these disadvantages [28,29].

Early second-order models for Newtonian fluids accounting for wall proximity, the so-called low Reynolds number Reynolds stress (RS) models, appeared in the 1970s [30,31]. To improve their performance in complex flows and better capture the anisotropic Reynolds stresses in the near-wall region, better near-wall closures were formulated in [32–34]. However, some of the earlier [27] and improved [30] near-wall closures were not asymptotically consistent and, to correct this deficiency, Lai and So [35] analysed in detail the anisotropic behaviour of the Reynolds stresses near the wall and developed an asymptotically correct near-wall RS closure, by improving the closures for the pressure redistribution and viscous dissipation. Based on the earlier investigations of Lai and So [35], Shima [36] incorporated an extra contribution to the production of ε in the rate of dissipation equation, which impacted favourably on the budgets of $\overline{u_i u_j}$. This issue had been found originally by Hanjalic and Launder [31], but Shima realised that the model proposed by them was not asymptotically correct near the wall. The model of Lai and So [35] captures well the RS anisotropy of Newtonian fluids in turbulent pipe flow, as also confirmed by Thakre and Joshi [37], who compared also their predictions with those of the model of Prud'homme and Elghobashi [33]. For convenience and given its good performance and simplicity, it is easier to adopt at this stage the model of Lai and So as the base for the second-order turbulence model for shear-thinning viscoelastic fluids, rather than select other more complex closures, such as the model of Craft [38].

The model of Craft [38] is an extension of the model of [39] and is also able to capture well the RS anisotropy. It is particularly suitable to recirculating flows and flows near walls with curvature and its predictions are in reasonable agreement with experimental and DNS data for Newtonian fluid flows. The advantage of Craft's model is its independence from wall-normal vectors and distances, thus allowing its easy use in complex geometries, at the expense of a rather complex formulation, so its adoption would imply more severe modifications to deal with viscoelastic fluids, whereas at this stage only fully developed channel flow is being considered, which does not require such a complex formulation. Note also that following a different approach, Shima [40] developed a simpler low Reynolds number second-moment closure and tested it in thin shear layer flows. Its overall performance was good, but its predictions of the normal Reynolds stresses in Newtonian turbulent channel flow were less accurate than those of Craft's model [38].

In this work a second-order RS model is developed for viscoelastic fluids described by the modified generalised Newtonian model of Pinho [7] and applied to predict fully developed turbulent channel flows of polymer solutions. The present RS closure is a step forward in the hierarchy of models for viscoelastic fluids and is built on top of the model of Lai and So [35] for Newtonian fluids. As hinted above, this base model was selected because it combines simplicity with a low Reynolds number capability, which is an essential requirement to deal with viscoelastic fluids for which no universal law of the wall exists. The performance of the model is tested against the experimental data-sets of Resende et al. [10] and Escudier et al. [41] for dilute aqueous solutions of polymers. Predictions by this turbulence model are also compared with DNS data obtained for viscoelastic fluids described by the FENE-P constitutive equation after an adequate comparison between the material functions of both the modified GNF and the FENE-P models.

The next section presents the governing equations for viscoelastic turbulent flow. The terms that require modelling are identified in Section 3 together with the development of the corresponding closures. The calibration of the model is made in Sections 4 and 5 for Newtonian and viscoelastic fluids, respectively. The results of the numerical simulations

and their discussion are presented in Section 6. The paper closes with a summary of the main conclusions.

2. Governing equations

In what follows overbars or upper-case letters denote Reynolds-averaged quantities and lower case letters are used for fluctuating quantities. The indicial notation of Einstein is used throughout the paper.

The Reynolds-averaged governing equations for incompressible fluids are the continuity equation:

$$\frac{\partial U_i}{\partial x_i} = 0, \tag{1}$$

and the momentum equation:

$$\rho \frac{\partial U_i}{\partial t} + \rho U_k \frac{\partial U_i}{\partial x_k} = -\frac{\partial \bar{p}}{\partial x_i} + \frac{\partial}{\partial x_k}\left(2\bar{\mu} S_{ik} - \rho\overline{u_i u_k} + 2\overline{\mu' s_{ik}}\right), \tag{2}$$

where p is the pressure, $\bar{\mu}$ is the average molecular viscosity, u_i is the ith component of the velocity vector and S_{ij} is the rate of deformation tensor defined as $S_{ij} \equiv \left(\partial u_i/\partial x_j + \partial u_j/\partial x_i\right)/2$.

This momentum equation is written down for a fluid described by a modified form of the GNF model, originally formulated in Pinho [7] and given in Equations (3) and (4):

$$\sigma_{ij} = \mu\left(\dot{\gamma}, \dot{\varepsilon}\right) S_{ij}, \tag{3}$$

$$\mu\left(\dot{\gamma}, \dot{\varepsilon}\right) = \underbrace{K_v \left[\dot{\gamma}^2\right]^{(n-1)/2}}_{\eta_v} \underbrace{K_e \left[\dot{\varepsilon}^2\right]^{(p-1)/2}}_{\eta_e^*}. \tag{4}$$

This constitutive equation incorporates non-Newtonian characteristics which are relevant to turbulent flow of viscoelastic fluids, such as the effect of strain-hardening extensional viscosity. The coefficients K_v and n are the consistency and exponent of the power-law fit of η_v to the shear viscosity data with $\dot{\gamma} = \sqrt{2 S_{ij} S_{ij}}$, an invariant of the rate of strain tensor. The dimensionless strain-hardening contribution (η_e^*) is defined as one-third of the non-dimensional Trouton ratio $\eta_e\left(\dot{\varepsilon}\right)/(3\eta_v\left(\dot{\gamma}\right))$, and the coefficients K_e and p represent fitting parameters to this quantity, which depend on the viscoelastic fluid rheology measurements. Here, the other invariant of the rate of strain tensor is quantified as $\dot{\varepsilon} = \dot{\gamma}/\sqrt{3}$, as explained in Barnes et al. [42]. More details of this model can be found in [7,8]. Note that in a pure shear flow Equation (4) reduces to the shear viscosity contribution, but in the presence of turbulent fluctuations it contains a non-unitary contribution from the extensional viscosity.

The momentum equation, Equation (2), contains the divergent of the molecular stress, of the Reynolds stress and of a new non-Newtonian stress, called the pseudo-elastic stress.

To determine the pseudo-elastic stress, $2\overline{\mu' s_{ik}}$, in the context of the second-order turbulence closure, a specific model needs to be developed, the subject of the next section. The average molecular viscosity ($\bar{\mu}$) is also affected by turbulence and the closure of Pinho [7] is used without modifications. It is given by Equation (5), which combines the pure viscometric viscosity contribution, η_v, defined in Equation (4) for a Reynolds-averaged shear rate

($\dot{\gamma}$), with the high Reynolds number Reynolds-averaged molecular viscosity contribution ($\bar{\mu}_h$) of Equation (6):

$$\bar{\mu} = f_v \bar{\mu}_h + (1 - f_v)\,\eta_v, \tag{5}$$

$$\bar{\mu}_h = \left(C_\mu \rho\right)^{3m(m-1)A_2/(8+3m(m-1)A_2)} \times 2^{4m(m-1)A_2/(8+3m(m-1)A_2)} \times k^{6m(m-1)A_2/(8+3m(m-1)A_2)} \times \varepsilon^{([8-3(m-1)A_2]m)/(8+3m(m-1)A_2)} \times B^{8/(8+3m(m-1)A_2)}, \tag{6}$$

where ε is the rate of dissipation of turbulent kinetic energy (k), and

$$m = \frac{n+p-2}{n+p} \text{ and } B = \left[\frac{K_v K_e}{A_\varepsilon^{p-1}}\right]^{1-m} 2^{[(n-1)-m(n+1)]/2} \rho^m. \tag{7}$$

The matching function f_v, defined in Equation (8), was made equal to the damping function f_μ, appearing in the eddy viscosity of the two-equation k–ε model of [8, 9]. The remaining coefficients take the values, $A_\varepsilon = 10$, $A_2 = 0.45$ and $C_\mu = 0.084$:

$$f_v = \left\{1 - \left[1 + \left|\frac{1-n}{1+n}\right| y^+\right]^{-\left|1+n/1-n\right|/A^+}\right\} \times \left\{1 - \left[1 + \left|\frac{p-1}{3-p}\right| y^+ C^{\frac{1-p}{2-p}}\right]^{-\left|3-p/p-1\right|/A^+}\right\}. \tag{8}$$

The RS tensor ($\rho\overline{u_i u_k}$) is determined via its transport equation (Equation (9)), which contains a large number of new terms on its right-hand side due to the non-Newtonian nature of the governing rheological constitutive equation. This exact equation, derived by Pinho [7], contains three sets of terms: first, those terms that are formally independent of the rheological constitutive equation, but that require modelling, which may depend on the fluid rheology (for instance, it is known from DNS that the addition of polymers affect turbulent diffusion and in particular the pressure strain term, [43]); second, the terms where the constant viscosity of the Newtonian fluids has been substituted by the Reynolds-averaged viscosity of the modified GNF model (terms IV, V) and finally, the new terms which are either associated to viscosity fluctuations or to spatial variations of the Reynolds-averaged viscosity (terms VI–XVII), here denoted as pseudo-elastic terms. The specific

modifications and new closures of this equation are discussed in Section 3.2,

$$\rho\frac{D\overline{u_iu_j}}{Dt}+\rho\overline{u_ju_k}\frac{\partial U_i}{\partial x_k}+\rho\overline{u_iu_k}\frac{\partial U_j}{\partial x_k}=-\rho\underbrace{\frac{\partial}{\partial x_k}\overline{u_iu_ju_k}}_{\text{I}}-\left(\underbrace{\frac{\partial}{\partial x_i}\overline{p'u_j}+\frac{\partial}{\partial x_j}\overline{p'u_i}}_{\text{II}}\right)$$
$$+\underbrace{\overline{p'\left(\frac{\partial u_j}{\partial x_i}+\frac{\partial u_i}{\partial x_j}\right)}}_{\text{III}}+\underbrace{\bar{\mu}\frac{\partial^2\overline{u_iu_j}}{\partial x_k\partial x_k}}_{\text{IV}}-\underbrace{2\bar{\mu}\overline{\frac{\partial u_i}{\partial x_k}\frac{\partial u_j}{\partial x_k}}}_{\text{V}}+\underbrace{\frac{\partial\bar{\mu}}{\partial x_k}\frac{\partial\overline{u_iu_j}}{\partial x_k}}_{\text{VI}}$$
$$+\frac{\partial\bar{\mu}}{\partial x_k}\left(\underbrace{\frac{\partial\overline{u_ku_j}}{\partial x_i}}_{\text{VII}}+\underbrace{\frac{\partial\overline{u_ku_i}}{\partial x_j}}_{\text{VIII}}-\underbrace{2\overline{u_ks_{ij}}}_{\text{IX}}\right)+\underbrace{\overline{\mu'\frac{\partial^2u_iu_j}{\partial x_k\partial x_k}}}_{\text{X}}-\underbrace{2\overline{\mu'\frac{\partial u_i}{\partial x_k}\frac{\partial u_j}{\partial x_k}}}_{\text{XI}}$$
$$+\underbrace{\overline{\frac{\partial\mu'}{\partial x_k}\frac{\partial u_iu_j}{\partial x_k}}}_{\text{XII}}+\underbrace{\overline{\frac{\partial\mu'}{\partial x_k}\left(u_j\frac{\partial u_k}{\partial x_i}+u_i\frac{\partial u_k}{\partial x_j}\right)}}_{\text{XIII}}+\underbrace{\overline{\mu'u_j}\frac{\partial^2U_i}{\partial x_k\partial x_k}}_{\text{XIV}}$$
$$+\underbrace{\overline{\mu'u_i}\frac{\partial^2U_j}{\partial x_k\partial x_k}}_{\text{XV}}+\underbrace{\overline{u_j\frac{\partial\mu'}{\partial x_k}\left(\frac{\partial U_i}{\partial x_k}+\frac{\partial U_k}{\partial x_i}\right)}}_{\text{XVI}}+\underbrace{\overline{u_i\frac{\partial\mu'}{\partial x_k}\left(\frac{\partial U_j}{\partial x_k}+\frac{\partial U_k}{\partial x_j}\right)}}_{\text{XVII}}. \tag{9}$$

3. Closures for non-Newtonian terms

3.1. *Momentum equation*

The momentum equation (2) contains two stress terms related to the variable viscosity, which require modelling. The stress, $2\bar{\mu}S_{ik}$, can be computed with the closure for the Reynolds-averaged molecular viscosity ($\bar{\mu}$) presented in the previous section, but the pseudo-elastic stress, $2\overline{\mu's_{ik}}$, must be modelled. Cruz et al. [9] proposed a closure for the pseudo-elastic stress in the context of their low Reynolds number k–ε model. Here, a different closure is developed to be consistent with the use of the full RS model, which incorporates the anisotropic nature of turbulence and its impact upon this stress component. To develop a closure for the pseudo-elastic stress tensor, we provide estimates of the fluctuating viscosity and strain rate tensors, on the basis of known quantities, and then combine them with a coefficient. From Equation (4), the fluctuating viscosity is proportional to

$$\mu'\propto K_vK_e(\dot{\varepsilon}')^{p-1}(\dot{\gamma}')^{n-1} \tag{10}$$

with

$$\dot{\gamma}'\sim\sqrt{s_{ij}s_{ij}}\text{ and }\dot{\varepsilon}'\sim\frac{\sqrt{s_{ij}s_{ij}}}{A_\varepsilon}, \tag{11}$$

where $\dot{\gamma}$ and $\dot{\varepsilon}$ are invariants of the fluctuating rate of strain tensors, and A_ε is an empirical parameter used to quantify the relation between shear rates and strain rates within the

flow [9]. Denoting $S \equiv \sqrt{s_{ij}s_{ij}}$ and back substituting

$$\mu' \propto \frac{K_v K_e}{A_\varepsilon^{p-1}} S^{p+n-2}. \tag{12}$$

Combining this with the fluctuating rate of strain tensor, one gets

$$\mu' s_{ij} \propto \frac{K_v K_e}{A_\varepsilon^{p-1}} S^{p+n-2} s_{ij}. \tag{13}$$

To arrive at closures for S and s_{ij} concepts of near-wall turbulence are invoked, specifically (1) that we are in the equilibrium region, where production of turbulence is balanced by its rate of dissipation and (2) that, as a first approximation, this balance is not affected significantly by the new pseudo-elastic stress. Similarly, we further assume that the rate of dissipation, $\rho\varepsilon$, is essentially equal to $2\bar{\mu}S^2$, i.e., for channel flow, one gets

$$P_k = -\rho\overline{uv}\frac{\partial U}{\partial y} \approx \rho\varepsilon \equiv 2\overline{\bar{\mu}s_{ij}^2} \sim 2\bar{\mu}S^2 \Rightarrow S^2 = \frac{-\rho\overline{uv}}{2\bar{\mu}}\frac{\partial U}{\partial y}. \tag{14}$$

We now generalise the shear stress and shear rate tensors of Equation (14) to the full tensor, considering also that $S^2 \geq 0$, to obtain

$$S^2 = \left| \frac{-\rho\overline{u_i u_j}}{4\bar{\mu}} S_{ij} \right|. \tag{15}$$

Within the boundary layers $s_{ij} \approx \partial u_i/\partial x_j$ and $u_i \sim \sqrt{\overline{u_i u_j}}$, thus s_{ij} can be calculated by

$$s_{ij} \sim \frac{\partial u_i}{\partial x_j} \sim \frac{u_i}{L_c}, \tag{16}$$

where L_c is an estimate of the spatial scales of turbulence. Here this length scale is given by the following expression developed in [9]:

$$\frac{1}{L_c} = \frac{\varepsilon}{u_R^3}, \tag{17}$$

where u_R is a turbulence velocity scale defined by

$$u_R^2 = \frac{k}{\left|\exp\left(-\left(k/u_\tau^2\right)^\alpha\right) - 1\right|^{1/\alpha}} \text{ with } \alpha = 2. \tag{18}$$

To conclude, the final expression for the pseudo-elastic stress in the context of a second-order turbulence closure is

$$2\overline{\mu' s_{ij}} = \tilde{C}\frac{K_v K_e}{A_\varepsilon^{p-1}} \left[\left| \frac{\rho\overline{u_i u_j}}{4\bar{\mu}} S_{ij} \right| \right]^{\frac{(p+n-2)}{2}} \times \frac{1}{L_c} \times \frac{\overline{u_i u_j}}{\sqrt{\left|\overline{u_i u_j}\right|}} \tag{19}$$

with

$$\tilde{C} = (1 + C_0)^{p+n-2} - 1. \tag{20}$$

The pseudo-elastic stress vanishes in the Newtonian limit ($n = 1$ and $p = 1$) as it should, an effect properly accounted for by parameter $\tilde{C}$, which depends on parameter C_0 to be quantified later.

3.2. *Reynolds stress transport equation*

The terms on the left-hand side of the RS transport equation (9) concern the time variation, the advection and the production of the Reynolds stress. They are all exact terms that do not require modelling, but on the right-hand side all terms need to be modelled. However, as mentioned at the end of Section 2, one set of terms is identical to those in the corresponding equation for Newtonian fluids (terms I–III), in the second set, the constant viscosity has been substituted by the Reynolds-averaged viscosity and only the third set contains new terms that do not exist for Newtonian fluids.

Even though the terms of the first two sets have differences relative to the corresponding Newtonian equation, they play a similar physical role, whereas the various terms of the third set are all new. Unfortunately, there are no DNS data for this modified GNF constitutive equation from which one could gather information as to the relevance of each term, but Pinho [7] performed an order of magnitude analysis of all terms of this transport equation to assess the relevance of the new terms in comparison to the terms found in the corresponding equation for Newtonian fluids, which is briefly reviewed here. In that analysis, the following scales were used: U was the velocity scale for the mean flow, $u \approx \sqrt{k}$ was the velocity scale for velocity fluctuations, L represented the large length scale for the mean flow and the energy containing eddies and l was the length scale associated with small fluctuations and its gradients. This small length scale is related to the Kolmogorov length scale, $\eta = (\bar{\nu}^3/\varepsilon)^{1/4}$, therefore, the ratio of small to large length scales is $l/L \sim (uL/\bar{\nu})^{-3/4}$, where the inviscid estimative of the rate of dissipation, $\varepsilon = u^3/L$, was used.

Since the viscosity is not constant it was also necessary to estimate the magnitude of the viscosity fluctuations and Pinho [7] arrived at

$$\frac{\nu'}{\bar{\nu}} \sim \left(\frac{uL}{\bar{\nu}}\right)^{3a/4} - 1, \tag{21}$$

where $a = 0.225m\,(m-1)$ and $m = (n + p - 2)/(n + p)$.

Table 1, adapted from [7], presents the estimate of the order of magnitude of each non-Newtonian term relative to the Newtonian dissipative term ($(2\bar{\mu}\overline{(\partial u_i/\partial x_k)(\partial u_j/\partial x_k)})$).

Inspection of Table 1 shows the need to model the largest terms of order 1, which are significantly larger than the others and always involve fluctuating viscosities. The terms in the fourth line involve viscosity fluctuations, but are otherwise alike to terms on the first line. Since these latter terms are of small magnitude they do not require modelling. Simultaneously, given the lack of information in the literature regarding the triple correlations of the derivatives of fluctuating viscosities, like terms in lines one, two and four were put together and closed as in Equations (22) and (23), introducing parameters

Table 1. Order of magnitude relative to the dissipative term (Reprinted from Journal of Non-Newtonian Fluid Mechanics, Vol. 114, Pinho, A GNF framework for turbulent flow models of drag reducing fluids and proposal for a k-ε type closure, Pages 149–184, Copyright (2003), with permission from Elsevier).

Term	Order	Estimate
$\frac{\partial \bar{\mu}}{\partial x_k}\left(\frac{\partial \overline{u_i u_j}}{\partial x_k}+\frac{\partial \overline{u_k u_j}}{\partial x_i}+\frac{\partial \overline{u_k u_i}}{\partial x_j}\right)$	$\left(\frac{uL}{\bar{\nu}}\right)^{-3/2}$	1×10^{-6}
$-\frac{\partial \bar{\mu}}{\partial x_k}2\overline{u_k s_{ij}}$	$\left(\frac{uL}{\bar{\nu}}\right)^{-3/4}$	1×10^{-3}
$\overline{\mu' \frac{\partial^2 u_i u_j}{\partial x_k \partial x_k}} - 2\overline{\mu' \frac{\partial u_i}{\partial x_k}\frac{\partial u_j}{\partial x_k}}$	$\left(\frac{uL}{\bar{\nu}}\right)^{3a/4}-1$	1
$\overline{\frac{\partial \mu'}{\partial x_k}\frac{\partial u_i u_j}{\partial x_k}} + \overline{\frac{\partial \mu'}{\partial x_k}\left(u_j\frac{\partial u_k}{\partial x_i}+u_i\frac{\partial u_k}{\partial x_j}\right)}$	$\left(\frac{uL}{\bar{\nu}}\right)^{3a/4}-1$	1
$\overline{\mu' u_j}\frac{\partial^2 U_i}{\partial x_k \partial x_k} + \overline{\mu' u_i}\frac{\partial^2 U_j}{\partial x_k \partial x_k}$	$\left[\left(\frac{uL}{\bar{\nu}}\right)^{3a/4}-1\right]\frac{U}{u}\left(\frac{uL}{\bar{\nu}}\right)^{-3/2}$	1×10^{-5}
$\overline{u_j \frac{\partial \mu'}{\partial x_k}\left(\frac{\partial U_i}{\partial x_k}+\frac{\partial U_k}{\partial x_i}\right)} + \overline{u_i \frac{\partial \mu'}{\partial x_k}\left(\frac{\partial U_j}{\partial x_k}+\frac{\partial U_k}{\partial x_j}\right)}$	$\left[\left(\frac{uL}{\bar{\nu}}\right)^{3a/4}-1\right]\frac{U}{u}\left(\frac{uL}{\bar{\nu}}\right)^{-3/4}$	1×10^{-3}

C_{V1} and C_{V2}, to be quantified later:

$$\frac{\partial \bar{\mu}}{\partial x_k}\frac{\partial \overline{u_i u_j}}{\partial x_k} + \overline{\frac{\partial \mu'}{\partial x_k}\frac{\partial u_i u_j}{\partial x_k}} \sim C_{V1}\times \frac{\partial \bar{\mu}}{\partial x_k}\frac{\partial \overline{u_i u_j}}{\partial x_k}, \tag{22}$$

$$\frac{\partial \bar{\mu}}{\partial x_k}\left(\frac{\partial \overline{u_k u_j}}{\partial x_i}+\frac{\partial \overline{u_k u_i}}{\partial x_j}-2\overline{u_k s_{ij}}\right) + \overline{\frac{\partial \mu'}{\partial x_k}\left(u_j\frac{\partial u_k}{\partial x_i}+u_i\frac{\partial u_k}{\partial x_j}\right)} \sim C_{V2}\times \frac{\partial \bar{\mu}}{\partial x_k}\left(\frac{\partial \overline{u_k u_j}}{\partial x_i}+\frac{\partial \overline{u_k u_i}}{\partial x_j}\right). \tag{23}$$

Extensive tests were made on the magnitude of these contributions to the transport equation of the RS and on their impact upon the predictions, and it was verified that here there was no need for any special near-wall treatment.

The diffusion-like triple correlation involving the fluctuating viscosity, the first term in the third line of Table 1, for which there is also lack of information, is added to the standard molecular diffusion of RS term (D_{ij}^{v}) and both are modelled together as in Equation (24):

$$\bar{\mu}\frac{\partial^2 \overline{u_i u_j}}{\partial x_k \partial x_k} + \overline{\mu' \frac{\partial^2 u_i u_j}{\partial x_k \partial x_k}} \approx \bar{\mu}\frac{\partial^2 \overline{u_i u_j}}{\partial x_k \partial x_k}. \tag{24}$$

The second term in the same third line is related to the fluctuating viscosity, but is otherwise very similar to the term V based on the Reynolds-averaged viscosity. The sum of both terms, in Equation (25), is here defined as the rate of dissipation tensor of the Reynolds

stresses, ε_{ij}, for the modified GNF model:

$$-2\bar{\mu}\overline{\frac{\partial u_i}{\partial x_k}\frac{\partial u_j}{\partial x_k}} - 2\overline{\mu'\frac{\partial u_i}{\partial x_k}\frac{\partial u_j}{\partial x_k}} = \rho\varepsilon_{ij}. \tag{25}$$

The rate of dissipation tensor needs to be modelled and this is achieved here considering turbulence anisotropy and near-wall effects related to the fluid rheology as in the model of Lai and So [35] of Equation (26), initially developed by Shima [36]. These are also related to the fluid rheology with the help of the damping function, $f_{w,1}$:

$$\varepsilon_{ij} = \frac{2}{3}\varepsilon\left(1 - f_{w,1}\right)\delta_{ij} + \frac{f_{w,1}\left(\varepsilon/k\right)\left[\overline{u_iu_j} + \overline{u_iu_k}n_kn_j + \overline{u_ju_k}n_kn_i + n_in_j\overline{u_ku_l}n_kn_l\right]}{1 + 3\overline{u_ku_l}n_ln_k/2k}. \tag{26}$$

The model for the rate of dissipation tensor of Equation (26) relies on the scalar isotropic rate of dissipation of turbulent kinetic energy ε, which is calculated by its own transport equation. The exact form of this transport equation is rather complex, even for Newtonian fluids and more so for non-Newtonian fluids, but in this model we will minimise the changes in relation to the closed form adopted by Lai and So [35], i.e., only the constant kinematic viscosity of Newtonian fluids is substituted by the Reynolds-averaged kinematic viscosity of the modified GNF model ($\bar{\nu}$):

$$\begin{aligned}\frac{D\varepsilon}{Dt} = {} & \frac{\partial}{\partial x_k}\left(\bar{\nu}\frac{\partial\varepsilon}{\partial x_k}\right) + \frac{\partial}{\partial x_k}\left(C_s\frac{k}{\varepsilon}\overline{u_ku_i}\frac{\partial\varepsilon}{\partial x_i}\right) + C_{\varepsilon_1}\left(1 + \sigma f_{w,2}\right)\frac{\varepsilon}{k}\tilde{P} \\ & - C_{\varepsilon_2}f_\varepsilon\frac{\varepsilon\tilde{\varepsilon}}{k} + f_{w,2}\left[\left(\frac{7}{9}C_{\varepsilon_2} - 2\right)\frac{\varepsilon\tilde{\varepsilon}}{k} - \frac{1}{2k}\left(\varepsilon - \frac{2\bar{\nu}k}{y^2}\right)^2\right].\end{aligned} \tag{27}$$

Equation (27) uses the pseudo-dissipation ($\tilde{\varepsilon}$) given by

$$\tilde{\varepsilon} = \varepsilon - 2\bar{\nu}\left(\frac{\partial k^{1/2}}{\partial x_y}\right)^2. \tag{28}$$

The other non-Newtonian terms in Table 1 are neglected in this model and the remaining terms of the transport equation of the Reynolds stresses are mathematically identical to those used in the context of Newtonian turbulence, i.e., they do not contain either the Reynolds-averaged or the fluctuating molecular viscosity. Nevertheless, it is known from DNS data for polymer solutions modelled by the FENE-P rheological constitutive equations (cf. [43]) that the turbulent diffusion and in particular the pressure strain are affected by drag reduction, especially close to the wall. Therefore, although we model these terms inspired by Lai and So [35], especially on what concerns the high Reynolds number contributions, modifications are implemented on the near-wall corrections, as discussed next.

The turbulent diffusion by velocity fluctuations, D_{ij}^T, is modelled as originally by Lai and So [35] in Equation (29):

$$-\rho\frac{\partial}{\partial x_k}\overline{u_iu_ju_k} = \rho\frac{\partial}{\partial x_k}\left\{C_s\frac{k}{\varepsilon}\left[\overline{u_iu_l}\frac{\partial\overline{u_ju_k}}{\partial x_l} + \overline{u_ju_l}\frac{\partial\overline{u_ku_i}}{\partial x_l} + \overline{u_ku_l}\frac{\partial\overline{u_iu_j}}{\partial x_l}\right]\right\}. \tag{29}$$

The two pressure fluctuation correlations, ϕ_{ij}^{*}, are the turbulent diffusion by pressure, ϕ_{ij}^{p}, and the pressure strain, ϕ_{ij}, the first and second terms on the right-hand side of Equation (30), respectively,

$$\phi_{ij}^{*} = -\underbrace{\left(\frac{\partial}{\partial x_i}\overline{p'u_j} + \frac{\partial}{\partial x_j}\overline{p'u_i}\right)}_{\phi_{ij}^{p}} + \underbrace{\overline{p'\left(\frac{\partial u_j}{\partial x_i} + \frac{\partial u_i}{\partial x_j}\right)}}_{\phi_{ij}}. \tag{30}$$

Usually ϕ_{ij}^{p} is neglected at high Reynolds number flows or incorporated as part of D_{ij}^{T}, but without any modification to the closure of D_{ij}^{T}, because ϕ_{ij}^{p} is negligible in comparison to D_{ij}^{T} according to Laufer [44]. The pressure strain ϕ_{ij} is responsible for the distribution of turbulent kinetic energy among its three normal components; therefore, it plays a crucial role since non-Newtonian fluids exhibit a more anisotropic distribution of normal Reynolds stresses than Newtonian fluids. The adequate modelling of the pressure strain thus requires a near-wall sub-model to capture correctly the behaviour of the Reynolds stresses next to the wall, in addition to a far from wall closure ($\phi_{ij,1}$). The adopted model for the pressure strain is given in Equation (31), where $\phi_{ij,w} f_{w,1}$ compensates for the shortcomings of $\phi_{ij,1}$ next to the wall, in particular, introducing the different behaviour of the RS according to the orientation of the flow and wall (for instance, the RS normal to the wall is subject to a stronger attenuation than the other two normal stress components), and additionally incorporating the strong rheological effects there via function $f_{w,1}$:

$$\phi_{ij}^{*} = \phi_{ij} = \phi_{ij,1} + \phi_{ij,w} f_{w,1}. \tag{31}$$

The idea behind this closure allows the turbulence model to handle successfully a wide range of complex flows and has been around at least since [30]. Here, we adopt for $\phi_{ij,1}$ and $\phi_{ij,w}$ the closures of Lai and So [35] for Newtonian fluids, presented in Equations (32) and (33):

$$\begin{aligned}\phi_{ij,1} = &-C_1\frac{\varepsilon}{k}\left(\overline{u_i u_j} - \frac{2}{3}k\delta_{ij}\right) - \alpha\left(P_{ij} - \frac{2}{3}\tilde{P}\delta_{ij}\right) - \beta\left(D_{ij} - \frac{2}{3}\tilde{P}\delta_{ij}\right)\\ &- \gamma k\left(\frac{\partial U_i}{\partial x_j} + \frac{\partial U_j}{\partial x_i}\right),\end{aligned} \tag{32}$$

$$\phi_{ij,w} = C_1\frac{\varepsilon}{k}\left(\overline{u_i u_j} - \frac{2}{3}k\delta_{ij}\right) - \frac{\varepsilon}{k}\left(\overline{u_i u_k}n_k n_j + \overline{u_j u_k}n_k n_i\right) - \alpha^{*}\left(P_{ij} - \frac{2}{3}\tilde{P}\delta_{ij}\right), \tag{33}$$

In Equations (32) and (33), the various quantities are given by

$$\begin{aligned}&P_{ij} = \left[\overline{u_i u_k}\frac{\partial U_i}{\partial x_k} + \overline{u_j u_k}\frac{\partial U_i}{\partial x_k}\right],\ D_{ij} = \left[\overline{u_i u_k}\frac{\partial U_k}{\partial x_j} + \overline{u_j u_k}\frac{\partial U_k}{\partial x_i}\right],\\ &\tilde{P} = \frac{1}{2}P_{ii},\quad \alpha = \frac{(8+C_2)}{11},\quad \beta = \frac{(8C_2-2)}{11},\quad \gamma = \frac{(30C_2-2)}{55}.\end{aligned} \tag{34}$$

The effect of Reynolds number on the pressure-strain model is taken care of by the damping function $f_{w,1}$ and here we do not adopt the function Lai and So [35], but use instead a new function that incorporates rheological effects also, namely the shear thinning of the shear viscosity and the strain hardening of the Trouton ratio. For this purpose, we rely

on a Van Driest type damping function ($f_{\mathrm{VD}} \propto \left(1 - \exp\left(-y^+/A\right)\right)^2$) [45] developed on the same principles as the eddy viscosity damping function of Cruz and Pinho [8], but further modified to take into account the stronger necessary damping of $\phi_{ij,w}$ required by the non-Newtonian fluids. This modification takes into account the contributions of the new viscoelastic terms in the governing equations and leads to a significant improvement over the previous k–ε turbulence model. In this RS model, the pseudo-elastic stress appearing in the momentum equation plays a more significant role there and in the energy budget. In the k–ε model, a significant proportion of the drag reduction was captured by the damping function of the eddy viscosity and the impact of the pseudo-elastic stress on the momentum equation was limited, whereas here the pseudo-elastic stress plays a more relevant role at the expense of the RS via the eddy viscosity. Simultaneously, we ensured that Newtonian fluid flow predictions remained equally accurate. The adopted function $f_{w,1}$ is given by Equation (35):

$$f_{w,1} = \exp\left[-\left(2.5\left\{1 - \left[1 + \left|\frac{1-n}{1+n}\right| y^+\right]^{-\left|1 + n/1 - n\right|/A^+}\right\} \times \left\{1 - \left[1 + \left|\frac{p-1}{3-p}\right| y^+ C^{\frac{1-p}{2-p}}\right]^{-\left|3 - p/p - 1\right|/A^+}\right\}\right)^{1.1}\right]. \tag{35}$$

The current turbulence model must remain valid for Newtonian fluids which are obtained by setting $n = 1$ and $p = 1$. In this case all non-Newtonian closures vanish, but the damping function $f_{w,1}$ does not revert to the form used by Lai and So [35], which relies on the turbulent Reynolds number R_T, whereas here the Reynolds number based on wall coordinates is being used ($y^+ = u_\tau y/\bar{\nu}_w$, where u_τ is the friction velocity). Predictions of the Newtonian turbulent channel flow with this modification are similar to those of Lai and So [35] model as assessed in Section 4.

Summarising, we put together all terms and the modelled transport equation for the RS tensor is given by

$$\begin{aligned}
&\rho\frac{D\overline{u_iu_j}}{Dt} + \rho\overline{u_ju_k}\frac{\partial U_i}{\partial x_k} + \rho\overline{u_iu_k}\frac{\partial U_j}{\partial x_k} \\
&\quad = \rho\frac{\partial}{\partial x_k}\left\{C_s\frac{k}{\varepsilon}\left[\overline{u_iu_l}\frac{\partial\overline{u_ju_k}}{\partial x_l} + \overline{u_ju_l}\frac{\partial\overline{u_ku_i}}{\partial x_l} + \overline{u_ku_l}\frac{\partial\overline{u_iu_j}}{\partial x_l}\right]\right\} \\
&\qquad + \underbrace{\phi_{ij,1} + \phi_{ij,w}f_{w,1}}_{\phi^*_{ij}} + \rho\varepsilon_{ij} + \bar{\mu}\frac{\partial^2\overline{u_iu_j}}{\partial x_k\partial x_k} \\
&\qquad + C_{V1}\frac{\partial\bar{\mu}}{\partial x_k}\frac{\partial\overline{u_iu_j}}{\partial x_k} + C_{V2}\times\frac{\partial\bar{\mu}}{\partial x_k}\left(\frac{\partial\overline{u_ku_j}}{\partial x_i} + \frac{\partial\overline{u_ku_i}}{\partial x_j}\right)
\end{aligned} \tag{36}$$

with the closure of ε_{ij} given by Equations (26)–(28) and the closure for ϕ^*_{ij} given by Equations (31)–(35). The turbulent Reynolds number R_T is here defined as $R_T = k^2/\bar{\nu}\varepsilon$.

4. Newtonian fluids simulations

The computer code used to carry out the numerical simulations for fully developed pipe flow is based on a finite-volume discretisation of the governing and turbulence model equations

Table 2. Coefficients and damping functions used by the Reynolds stress model (as in Lai and So's model [35]).

Constants					
$C_1 = 1.5$	$C_2 = 0.4$	$\alpha^* = 0.45$	$C_{\varepsilon_1} = 1.35$	$C_{\varepsilon_2} = 1.8$	$C_s = 0.11$
Damping functions					
$f_{w,2} = \exp\left[-\left(\frac{R_T}{64}\right)^2\right]$	$f_\varepsilon = 1 - \left(\frac{2}{9}\right)\exp\left[-\left(\frac{R_T}{6}\right)^2\right]$				

using staggered meshes and second-order central differences. The Tri-Diagonal Matrix Algorithm (TDMA) solver is used to calculate the solution of the discretised algebraic governing equations. The mesh is non-uniform with 199 cells across the pipe, giving mesh-independent results for Newtonian and non-Newtonian fluids within 0.1%. The full domain is mapped exclusively in the transverse direction, hence only the following wall boundary conditions need to be imposed:

$$U_i = 0; \quad \overline{u_i u_j} = 0 \text{ and } \varepsilon = 2\bar{\nu}\left(\frac{\partial k^{1/2}}{\partial y}\right)^2 \text{ at } r = R.$$

As explained at the end of Section 3.2, the damping function for the pressure strain ($f_{w,1}$) is new to accommodate both low Reynolds number and rheology effects. Even though this new function does not reduce to the same form as the function of Lai and So [35] for Newtonian fluids, it is necessary to ensure that under those conditions its predictions are at least as good as those of the Lai and So's [35] model in fully developed turbulent pipe flow. To ensure this, the damping function was calibrated with the numerical value of the coefficient $A^+ = 35$.

The coefficients and functions of the model presented in Table 2 take on the same values as Lai and So's model [35].

Simulations were carried out with both the present model and the original model of Lai and So [35] and compared with the extensive data-set of Durst et al. [46] pertaining to a Reynolds number of 7340. Further simulations were performed at three higher values of the Reynolds number just to compare the predictions of the friction factor with the values given by the Colebrook equation for smooth pipe (Eq. 37):

$$\frac{1}{\sqrt{f}} = -2.0\log_{10}\left[\frac{2.51}{\mathrm{Re}\sqrt{f}}\right]. \tag{37}$$

Table 3. Darcy friction factor for Newtonian pipe flow. Comparison between Colebrook equation (37) and the predictions by this model and the Lai and So's model [35].

Re	7,430	13,450	21,490	33,530
f_{Co} – Colebrook equation	0.03345	0.02858	0.02543	0.02288
f_{LS} – Lai and So's model	0.03755	0.03066	0.02622	0.02323
f – present model	0.03673	0.03006	0.02578	0.02279
$(f_{LS} - f_{BI})/f_{BI}(\%)$	12.23	7.24	3.09	1.52
$(f - f_{BI})/f_{BI}(\%)$	9.85	5.14	1.36	−0.39
$(f - f_{LS})/f_{LS}(\%)$	−2.2	−2	−1.7	−1.9

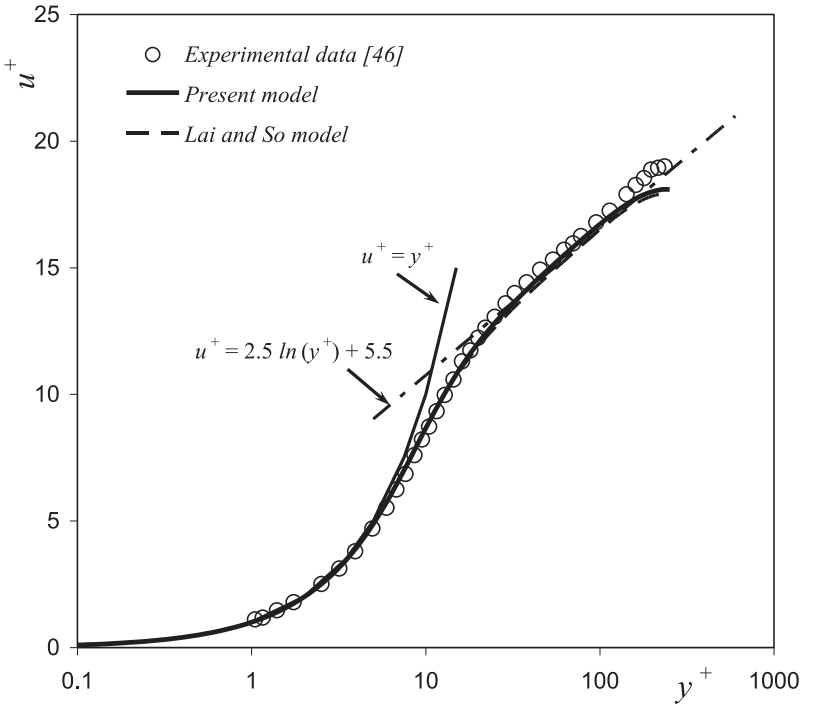

Figure 1. Comparison between the predicted and the measured mean velocity profile for fully developed turbulent pipe flow of Newtonian fluid at Re = 7430 in wall coordinates.

Table 3 compares the data and predictions of the Darcy friction coefficient and the differences between predictions by this model and by Lai and So's model are of the order of 2%. In relation to the Colebrook equation, the differences are larger at low Reynolds numbers, both for this model and for Lai and So's model. The small difference between the predictions of this model and of Lai and So's model have a corresponding small difference in the predictions of the mean velocity profiles in wall coordinates shown in Figure 1. At larger Reynolds numbers, our model approaches Lai and So's model predictions even better, with differences in the velocity profiles becoming negligible, but these are not shown here for conciseness.

The corresponding profiles of the normalised turbulent kinetic energy and Reynolds normal stresses are shown in Figure 2, which includes the experimental data from Durst et al. [46]. These turbulent quantities are normalised using the friction velocity (u_τ) as in Equation (38):

$$u'^+ = \sqrt{\overline{u^2}}\Big/u_\tau; \quad v'^+ = \sqrt{\overline{v^2}}\Big/u_\tau; \quad w'^+ = \sqrt{\overline{w^2}}\Big/u_\tau. \tag{38}$$

Actually, predictions of u'^+ by this model are closer to the experimental data than those of Lai and So's closure [35] and this also improves the predictions of k^+.

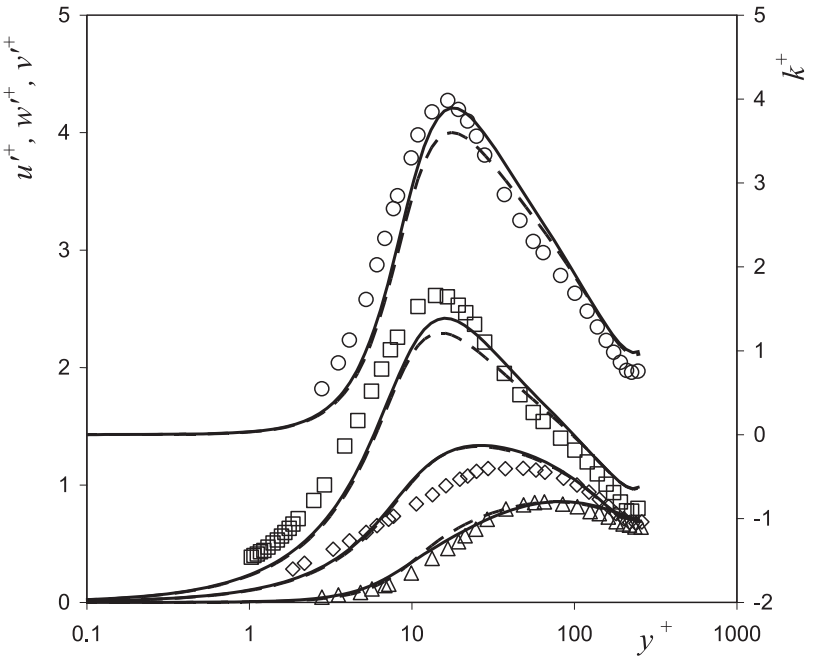

Figure 2. Comparison between the predicted (lines) and the measured (symbols) profiles of normalised turbulent kinetic energy and Reynolds normal stresses for fully developed turbulent pipe flow of Newtonian fluid at Re = 7430 in wall coordinates: ○ k^+, □ u'^+, ◇ w'^+, Δ v'^+ data [46]; — present model; - - Lai and So's model [35].

5. Calibration of the viscoelastic model

The turbulence model was calibrated first to predict well the turbulent channel flow of Newtonian fluids, as was described in the previous section, since some changes were made to the original closures of Lai and So [35]. Then, as described next, it was calibrated for the viscoelastic fluids using experimental data from a single fluid, an aqueous solution of polyacrylamide (PAA) at 0.125% by weight concentration taken from Escudier et al. [41]. Subsequently, without changing the turbulence model its performance is assessed in Section 6 for the remaining three viscoelastic fluids made from aqueous solutions of xanthan gum (XG), carboxymethylcellulose sodium salt (CMC) and a combination of XG and CMC at various weight concentrations. Specifically, the following solutions were used: 0.2% XG, 0.25% CMC and 0.09%/0.09% XG/CMC. The viscosity parameters in the modified GNF model of Equation (4) are presented in Table 4 for all fluids. These are the same as used previously in [9,10], and were obtained from the experimental shear and extensional viscosity measurements of Escudier et al. [41].

Table 4. Parameters of the viscosity model (cf. [9]).

Fluid	K_V (Pa.s^n)	n	K_e	p
0.25% CMC	0.2639	0.6174	2.0760	1.2678
0.09% CMC/0.09% XG	0.15178	0.5783	2.1833	1.1638
0.2% XG	0.2701	0.4409	3.8519	1.2592
0.125% PAA	0.2491	0.425	8.25	1.4796

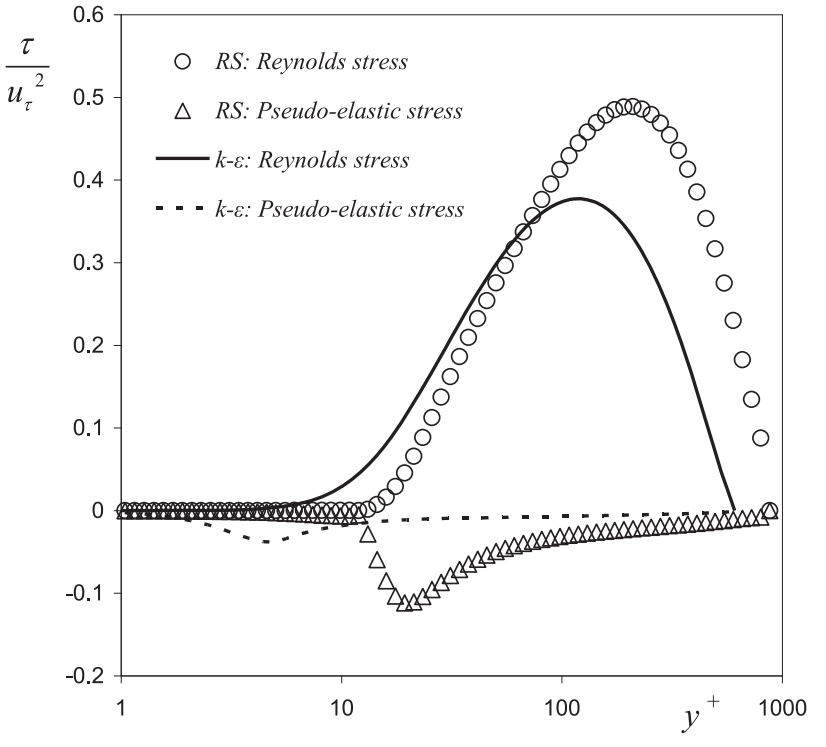

Figure 3. Variation across the pipe of the shear components of pseudo-elastic viscoelastic stress, defined by Equations (19) and (20), and of the Reynolds stress, in the context of the Reynolds stress model (symbol Δ) and the k–ε model (dashed line - - -), for 0.125% PAA fluid in turbulent pipe flow at Re = 42,900.

The coefficients of the viscoelastic turbulence model were quantified by an extensive parametric investigation to assess the impact of its various contributions to the performance of the model. First, we compare in Figure 3 the predictions of the pseudo-elastic stress by the RS model with those of the previous k–ε model for the same flow of 0.125% PAA. For reference, the predictions by both models of the corresponding shear RS are included. The pseudo-elastic stress in the momentum equation predicted by the RS model is larger by a factor of 3 than that of the former model, but what is more relevant is that this pseudo-elastic stress is important well within the buffer layer, whereas in the previous model the pseudo-elastic stress only existed inside the viscous sub-layer and in the lower buffer layer, an unlikely feature for a turbulent quantity. Additionally, the larger pseudo-elastic stress in the buffer layer allows for larger drag reductions. This is achieved here through an optimisation of the RS distribution and as a consequence the coefficient C_0 of the pseudo-elastic stress, defined by Equations (19) and (20), takes the new numerical value of $C_0 = -0.95$, which is slightly different from the value used in the context of the k–ε model of Cruz et al. [9]. Simultaneously, the new value of C in the viscoelastic damping function (Equation (35)) became $C = 25$, which is three times smaller than the value used in the previous k–ε model. These changes are related to the fact that in this RS model we imposed the maximum possible contribution from this pseudo-elastic stress while reducing the role of the viscoelastic damping function, which was taking most of the viscoelastic effects in the previous k–ε model. Note that the viscoelastic terms related to coefficients C_{V1} and C_{V2}

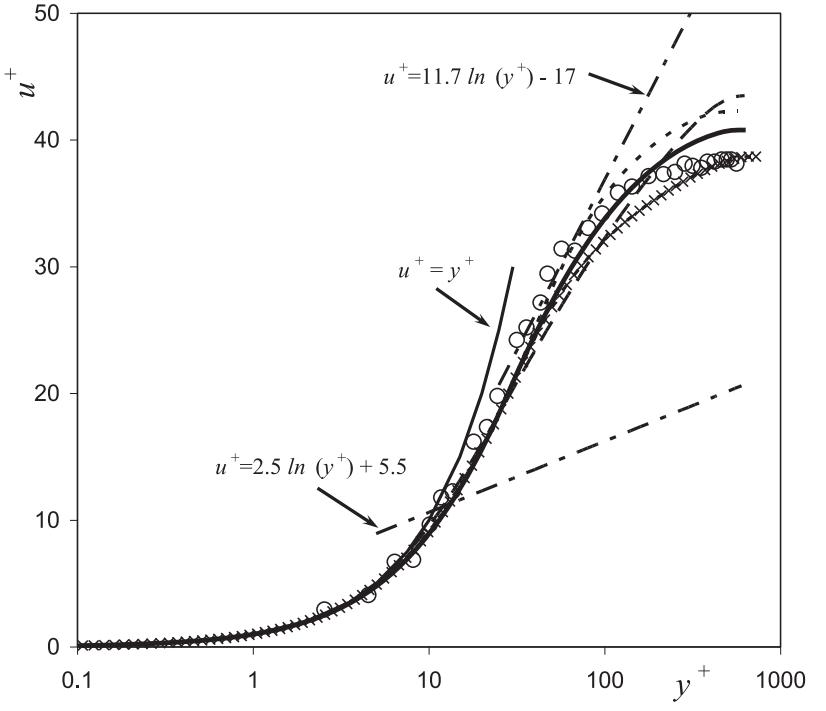

Figure 4. Comparison between the predicted (lines) and measured (symbols) mean velocity profile for fully developed turbulent pipe flow with the 0.125% PAA solution at Re = 42,900 in wall coordinates: ○ [41]; - × - present model with $C_{V1} = 0$; - - - present model with $C_{V2} = 0$; — present model; – – k–ε model [10].

also took over some of the viscoelastic contributions, but due to a lack of information on the distribution of turbulent energy among the various terms, we chose to maximise the role of elastic contribution via the pseudo-elastic term. For this reason, the coefficient C_{V1} of the viscoelastic term in Equation (22) was set to $C_{V1} = -1.7$, keeping the same sign of the pseudo-elastic stress but with a major impact away from the wall.

Even though this term contributes to all components of the RS tensor, for the pipe flow of 0.125% PAA at Re = 42,900, its main contribution is to the streamwise normal and shear components. In contrast, the contribution of the similar viscoelastic closure of Equation (23) is to the transverse and spanwise normal components, and here $C_{V2} = 0.2$. These two closures are used to improve the global behaviour of the turbulence model and that can be assessed in Figure 4, where predictions of the main velocity profiles are shown in wall coordinates for the 0.125% PAA turbulent pipe flow at Re = 42,900 with and without the C_{V1} and C_{V2}terms, and compared also with the prediction by the nonlinear k–ε model of Resende et al. [10]. There is clearly an improvement by the use of the RS model. Note that the data for the 0.125% PAA solution and the corresponding prediction are close to Virk's maximum drag reduction asymptote for the velocity (MDRA) [47], given by Equation (39), corresponding to a drag reduction of 60%–70%,

$$u^+ = 11.7 \ln\left(y^+\right) - 17. \tag{39}$$

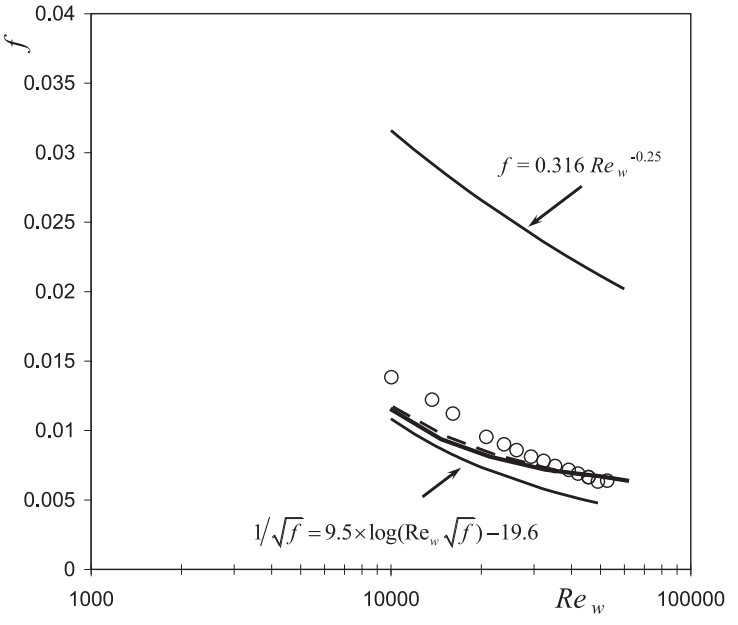

Figure 5. Comparison between predictions and measurements of Darcy friction factor in wall coordinates for fully developed turbulent pipe flow with 0.125% PAA fluid: ○ experimental data [41]; — present model; - - k–ε model [10].

The predicted variation of the Darcy friction factor with Reynolds number for the 0.125% PAA solution can be observed in Figure 5, which includes the Colebrook equation (37) for the Newtonian friction factor and MDRA equation (40):

$$1/\sqrt{f} = 9.5 \times \log\left(\mathrm{Re}_w\sqrt{f}\right) - 19.06. \tag{40}$$

The predictions compare well with the experimental data, but all models tend to underpredict f as the Reynolds number is reduced so that there is a difference of about 16% at $\mathrm{Re} = 10{,}000$. According to Resende et al. [10], the 0.125% PAA solution is a highly elastic fluid with a large drag reduction approaching Virk's MDRA.

The predicted profiles of the various normal Reynolds stresses (RSs) and the corresponding experimental data of Resende et al. [10] are compared in Figure 6, which also includes the corresponding turbulent kinetic energy profiles and also the predictions by the nonlinear k–ε model of Resende et al. [10]. As we can see, the present RS model underpredicts k and $\overline{u^2}$ near the wall, especially in the region of the peak stress. The prediction of $\overline{w^2}$ is good, but there is also an underprediction of $\overline{v^2}$, near and away from the wall. Therefore, the variations of the RS with the polymer additive are captured by the present RS turbulence model, but not so well as by the k–ε nonlinear model of Resende et al. [10]. This is so because in developing this RS model we kept the modifications of the Lai and So's model to a minimum, and essentially only one damping function was changed. In contrast, in the anisotropic k–ε model of Resende et al. [10], several damping functions were used and the authors were thus able to match more closely the experimental and numerical data, but this also suggests that the model of Resende et al. [10] is less robust than this RS model. Nevertheless, and in spite of the minimal number of changes made in the present model, the shift of the location of peak turbulence away from the wall is captured, but this came at

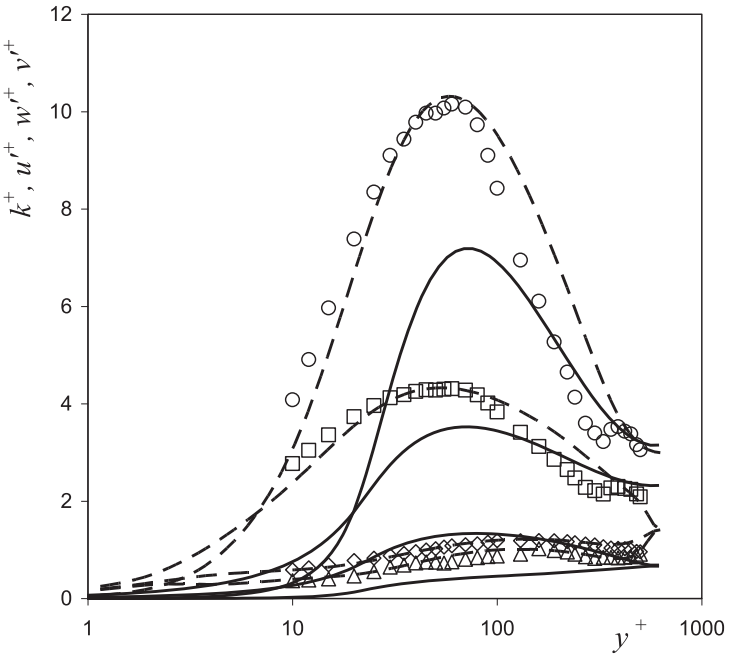

Figure 6. Comparison between the predicted (lines) and the measured (symbols) profiles of normalised turbulent kinetic energy and Reynolds normal stresses for fully developed turbulent pipe flow of 0.125% PAA fluid at Re = 42,900 in wall coordinates: ○ k^+ data [41]; □ u'^+, ◇ w'^+, Δ v'^+ data [10]; — present model; - - k–ε model [10].

the expense of an increased dissipation of the turbulence leading to a reduction of the peak value of k.

In Figure 7, the distributions of the various shear stresses are plotted for the 0.125% fluid. The predictions by the RS model (symbols) are different from those of the nonlinear k–ε model of Resende et al. [10], especially for the pseudo-elastic stress in the buffer layer. The pseudo-elastic stress is larger leading to an increase in the average molecular stress in the buffer layer to compensate and improve significantly the performance of the present turbulence model relative to the previous k–ε models.

In this RS model, the pseudo-elastic stresses are larger than in the model Cruz and Pinho [9], but they are still negative. This negative stress is not a deficiency of the model as deduced from the following reasoning: considering the total extra stress from a more fundamental point of view as the sum of a polymer contribution with a Newtonian solvent contribution ($\tau_t = \tau_p + \tau_s$), and since the modified GNF model does not make directly this separation, the polymer contribution to the total extra stress has to be computed by subtracting from the total stress the Newtonian solvent contribution, leading to the following result for the shear stress component:

$$\tau_p = 2\bar{\mu} S_{xy} + 2\overline{\mu' s_{xy}} - 2\mu_s S_{xy}, \tag{41}$$

where μ_s is the solvent viscosity. The transverse variations of τ_p, $-\rho\overline{u'v'}$ and τ_s are plotted in Figure 8 for the same case of Figure 7, i.e., for 0.125% PAA. The flow corresponds to the maximum drag reduction (DR) regime (60% < DR < 70%) with DR = 69% for 0.125% PAA at Re = 42,900, and the variation of those stresses across the pipe is qualitatively

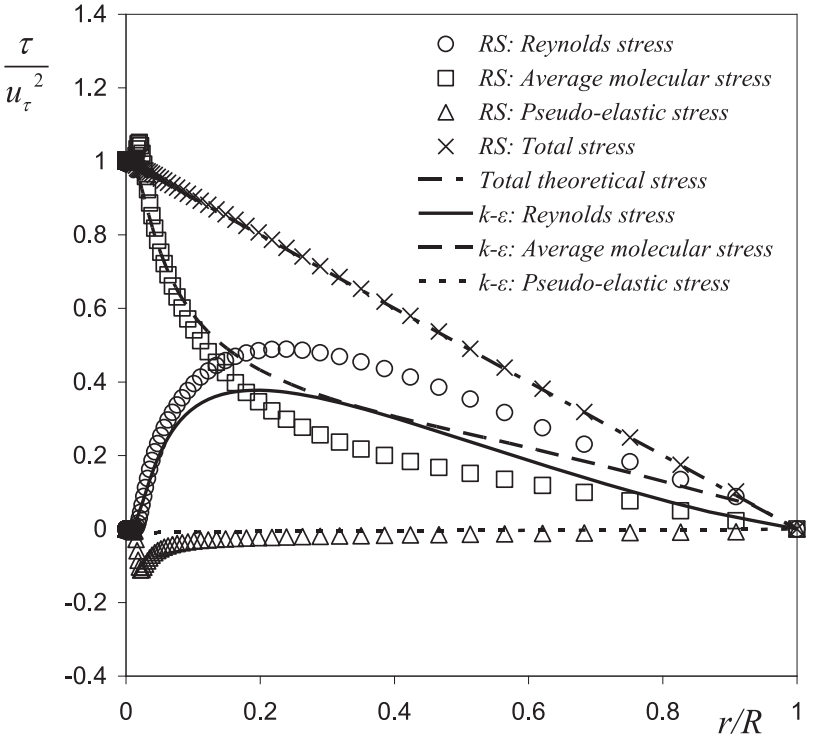

Figure 7. Comparison between the predictions of the various shear stress profiles by the Reynolds stress (RS) and k–ε turbulence models for pipe flow of 0.125% PAA at Re = 42,900.

similar to those seen by Ptasinski et al. [25] in their turbulent pipe flow experiments with other viscoelastic fluids. It also compares with the k–ε model predictions, where both models behave similarly next to wall. Across the pipe, we observe a shift away between the predictions by the RS and k–ε models of the shear Reynolds and polymeric stresses, but due to the lack of independent detailed information it is impossible to quantify the error predictions of the models. In both cases, the polymer shear stress remains positive and increases with drag reduction as it should. Additionally, when added to the positive solvent shear stress and to the positive Reynolds shear stress, the latter contribution decreasing with DR, the total shear stress now varies linearly across the pipe flow as it must from the momentum equation balance and regardless of the assumptions used to model the flow.

The various non-Newtonian terms of the momentum and RS equations affect different flow regions. The pseudo-elastic stress directly affects the buffer layer, but this is sufficient to change the flow across the whole pipe and it is especially important to create drag reduction. Indeed, and in contrast to the earlier $k-\varepsilon$ model of Cruz and Pinho [9], where the drag reduction was basically achieved by a reduction of the eddy viscosity, and the pseudo-elastic stress played a small role, this RS model has a more correct behaviour because the drag reduction is achieved by the increasing importance of the polymer stress (τ_p) and not just by a reduction of the RS, in agreement with experimental and DNS investigations for viscoelastic fluids (e.g., [11,25]). In the context of the rheological model used here, this is achieved also via the pseudo-elastic stress (cf. Equation (41)) and not exclusively by $2\bar{\mu}S_{ij}$. Additionally, the RS turbulence model captures the increased turbulence anisotropy, and

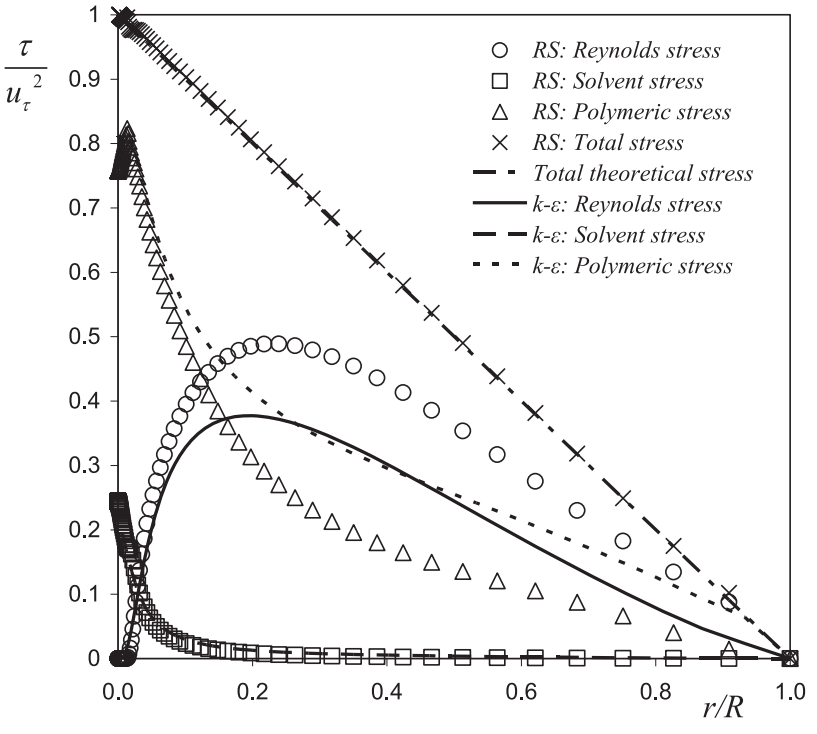

Figure 8. Radial distribution of the various shear stresses predictions by the Reynolds stress (RS) and k–ε turbulent models, for pipe flow of 0.125% PAA at Re = 42,900.

in particular, the reduction in the transverse normal RS which is usually associated with drag reduction. As the pseudo-elastic stress increases with drag reduction, there is also an increase of k^+, which represents an additional improvement over the k–ε closure of Cruz et al. [9].

6. Results and discussion

Following the calibration of the model against the experimental data-set of Escudier et al. [41] for the aqueous solution of 0.125% PAA, the performance of the developed RS model is now assessed against experimental data for three other different fluid flows. This is done both in terms of the predictions of the friction factor, but also in terms of profiles of the mean and turbulent velocities.

For the 0.25% CMC solution, the predictions of f as a function of the Reynolds number and of the mean and turbulent velocities at Re = 16,600 are presented in Figures 9–11, respectively. The slope of the predicted f–Re curve is lower than that of the experiments only by a small amount and the mean velocity profile shows also a good agreement with the experiments. In terms of the turbulent quantities, these are well predicted in terms of magnitude, but the locations of the predicted peak axial normal stress and k are shifted to higher values of y^+. Comparing with the k–ε model of Resende et al. [10], next to the wall there is an underprediction in all components of the RS tensor, but not so intense as occurs in the 0.125% PAA fluid. Across the pipe we obtained similar behaviour with the exception of the $\overline{v^2}$ underprediction and a small improvement in the $\overline{u^2}$ component.

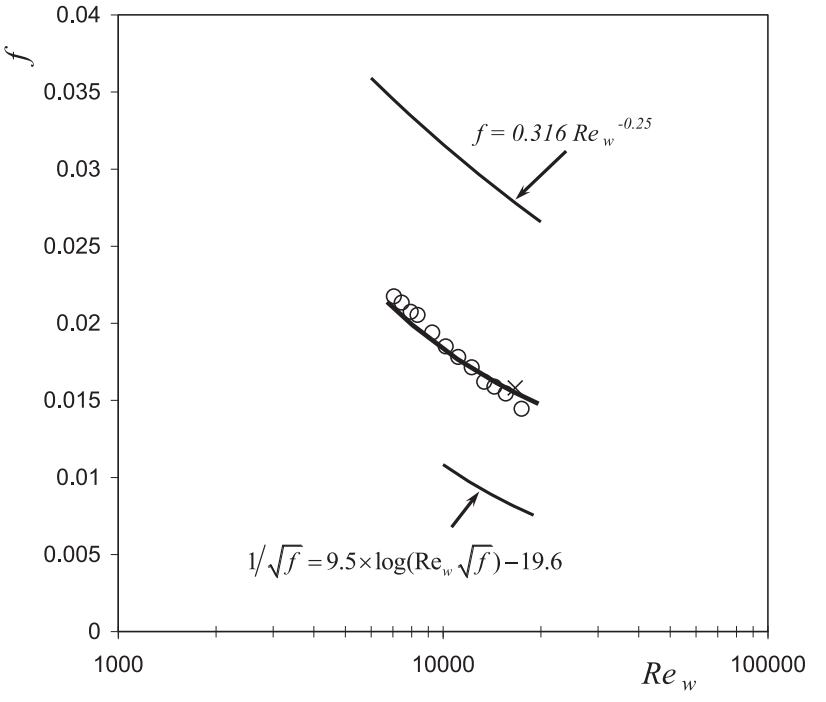

Figure 9. Comparison between predictions and measurements of Darcy friction factor in wall coordinates for fully developed turbulent pipe flow with 0.25% CMC fluid: ○ experimental data [41]; — present model; × k–ε model [10].

The predictions of the Darcy friction factor for the two aqueous polymer solutions based on XG, the blend of 0.09% CMC with 0.09% XG and the 0.2% XG solution, match very well with the experimental data as shown in Figures 12 and 13. For the blend, there is a 16% difference in the value of f at Re = 52,400, which decreases at lower Reynolds numbers. The opposite variation is observed to occur with the 0.2% XG fluids; now there is a 9% difference between the predicted and the experimental f at Re = 15,000, which decreases with increasing Reynolds numbers.

It must be emphasised at this stage that the predictions for these two fluids, and in particular for the 0.2% XG solution, are significantly better than was previously achieved by any of the linear two-equation closures developed in the past for viscoelastic fluids [8–10], and in particular, by the anisotropic k–ε model of Resende et al. [10]. This is an important achievement of the current RS model as is clear from the previous and subsequent plots, which include the predictions by the nonlinear k–ε model.

The corresponding predictions of the mean velocity and of the normal Reynolds stresses for the blend (0.09%/0.09% CMC/XG) and the 0.2% XG solutions, at Re = 45,200 and 39,000, respectively, match the experimental data. This is shown in Figures 14 and 15 for the blend, and in Figures 16 and 17 for the 0.2% XG solution. The predictions are better than those by the previous model of Resende et al. [10] with significant improvements, especially for the 0.2% XG solution for which the previous models were not particularly successful. Note that the flow of this solution of 0.2% XG is in the regime of maximum drag reduction. As for the previous two non-Newtonian fluids, the axial and radial Reynolds normal stresses and k are underpredicted near the wall. For the 0.2% XG solution, the

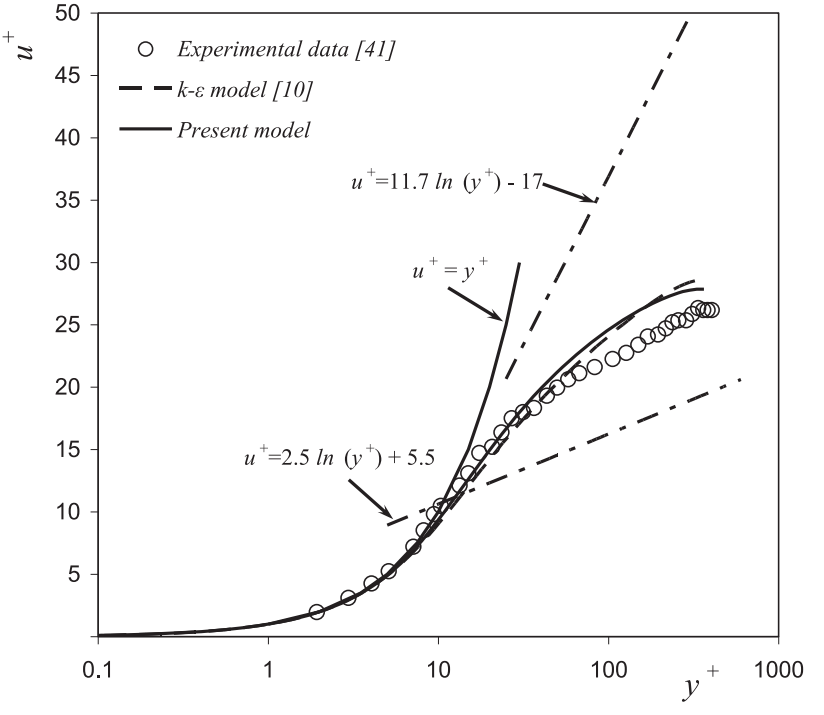

Figure 10. Comparison between the predicted and measured mean velocity profile for fully developed turbulent pipe flow with the 0.25% CMC solution at Re = 16,600 in wall coordinates.

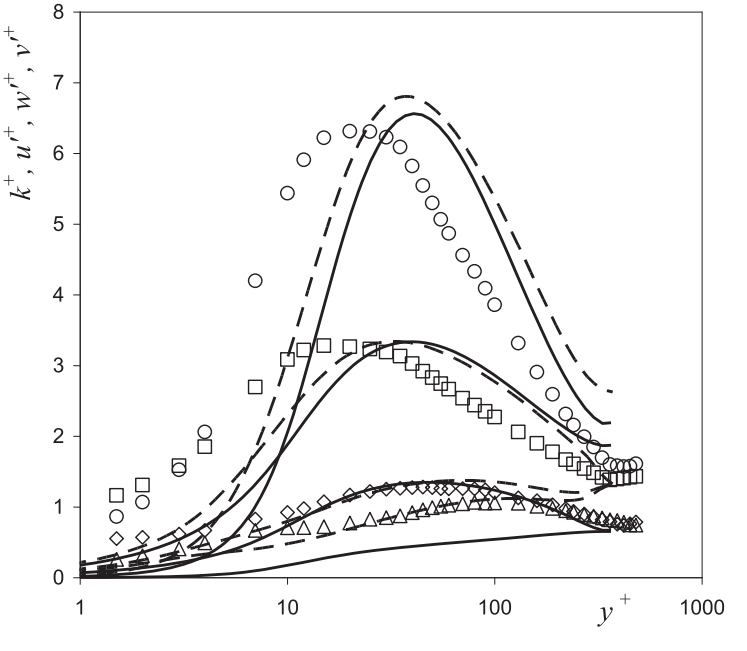

Figure 11. Comparison between the predicted (lines) and the measured (symbols) profiles of normalised turbulent kinetic energy and Reynolds normal stresses for fully developed turbulent pipe flow of 0.25% CMC fluid at Re = 16,600 in wall coordinates: ○ k^+ data [41]; □ u'^+, ◇ w'^+, Δ v'^+ data [10]; — present model; - - *k*–*ε* model [10].

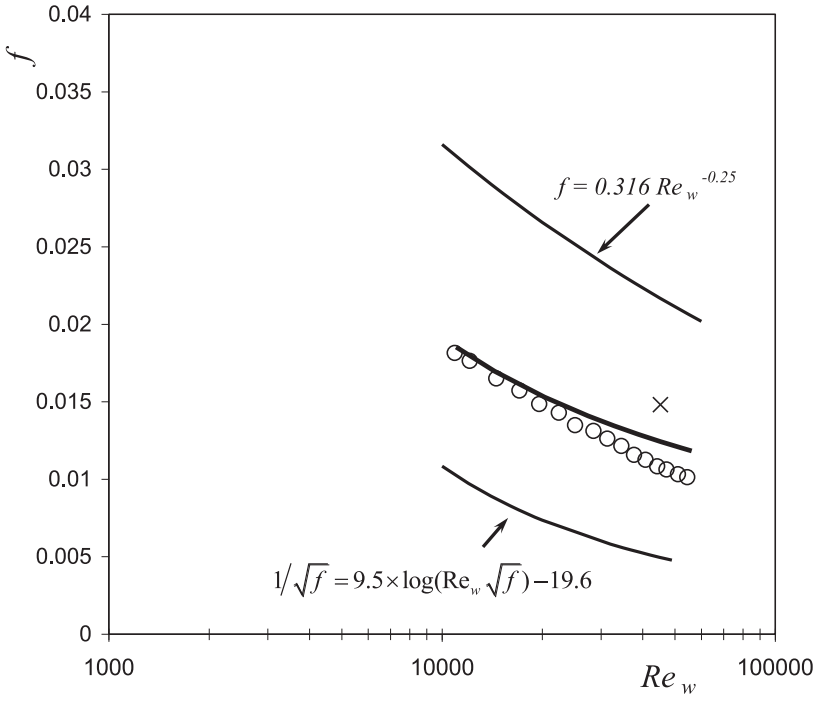

Figure 12. Comparison between predictions and measurements of Darcy friction factor in wall coordinates for fully developed turbulent pipe flow with 0.09%/0.09% CMC/XG fluid: ○ experimental data [41]; — present model; × k–ε model [10].

tangential Reynolds normal stress is slightly over-predicted. In addition, there is almost always an underprediction in k, $\overline{u^2}$ and $\overline{v^2}$ near the wall, whereas $\overline{w^2}$ is usually well predicted.

The shear stress distributions for the 0.2% XG solution can be observed in Figure 18, which can be compared with that of the 0.125% PAA solution (cf. Figure 7). Both flows belong to the maximum drag reduction regime (DR = 60.3% for 0.2% XG at Re = 39,000 and DR = 69% for 0.125% PAA at Re = 42,900). The profile of the pseudo-elastic stress of 0.2% XG is qualitatively similar to that of the 0.125% PAA solution acting essentially in the buffer layer, but with a higher magnitude, which is necessary to correct the previous failure of the k–ε model in predicting the velocity field, as mentioned before. This confirms that in the context of the RS model, the closure of the new pseudo-elastic stress model is significantly better than the closure of Cruz and Pinho [9] used in the context of the k–ε turbulence models. As for the 0.125% PAA in Figures 8 and 19, it plots the distribution of all relevant shear stresses across the pipe for the 0.2% XG solution. Again, the behaviour is alike that for the viscoelastic fluids of Ptasinski et al. [25] at maximum drag reduction (the 103 wppm, Weight Parts per Million, solution of Superfloc A110 with DR = 63% in their Figure 11), except for the proportion of the total stress distribution between the solvent and the polymer close to the wall. This difference stems from the fact that in Ptasinski et al. [25] the polymer solution is dilute whereas here the viscosity model was fit to the fluid rheology and the 0.2% XG is well above the critical concentration for the dilute regime, and for that reason the 50% distribution of the wall stress between solvent and polymer is reasonable.

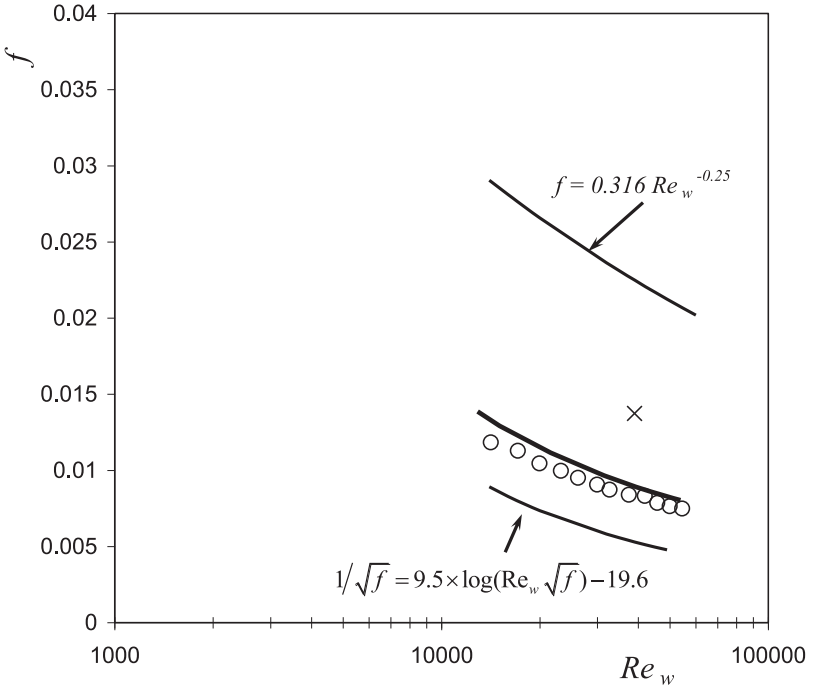

Figure 13. Comparison between predictions and measurements of Darcy friction factor in wall coordinates for fully developed turbulent pipe flow with 0.2% XG fluid: ○ experimental data [41]; — present model; × k–ε model [10].

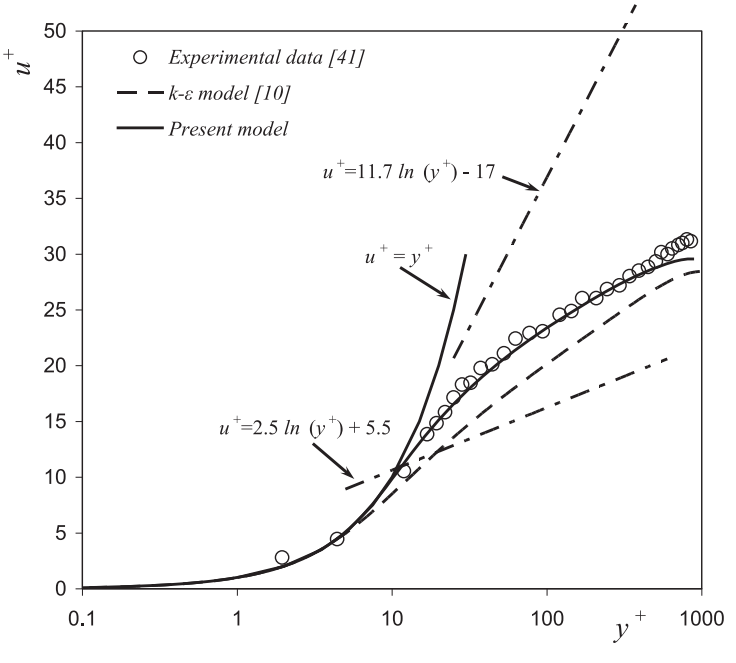

Figure 14. Comparison between the predicted and measured mean velocity profile for fully developed turbulent pipe flow with the 0.09%/0.09% CMC/XG solution at Re = 45,300 in wall coordinates.

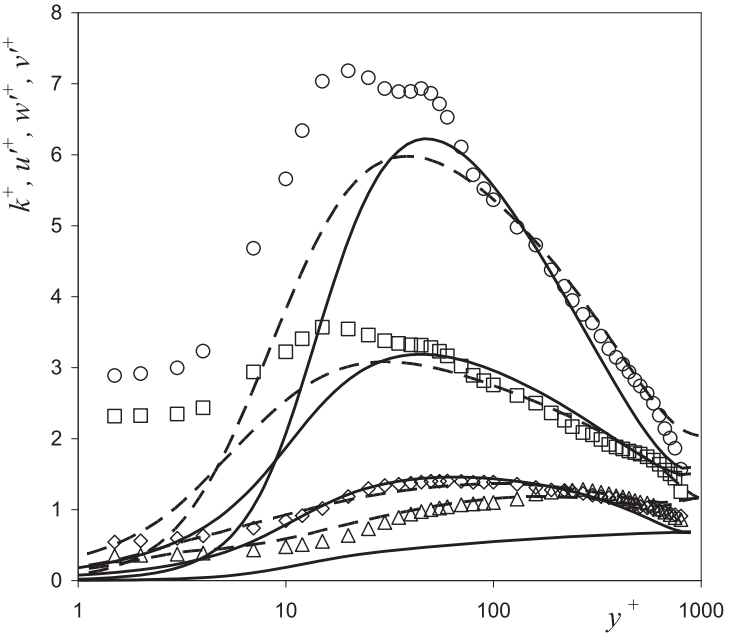

Figure 15. Comparison between the predicted (lines) and the measured (symbols) profiles of normalised turbulent kinetic energy and Reynolds normal stresses for fully developed turbulent pipe flow of 0.09%/0.09% CMC/XG fluid at Re = 45,300 in wall coordinates: ○ k^+ data [41]; □ u'^+, ◇ w'^+, Δ v'^+ data [10]; — present model; - - k–ε model [10].

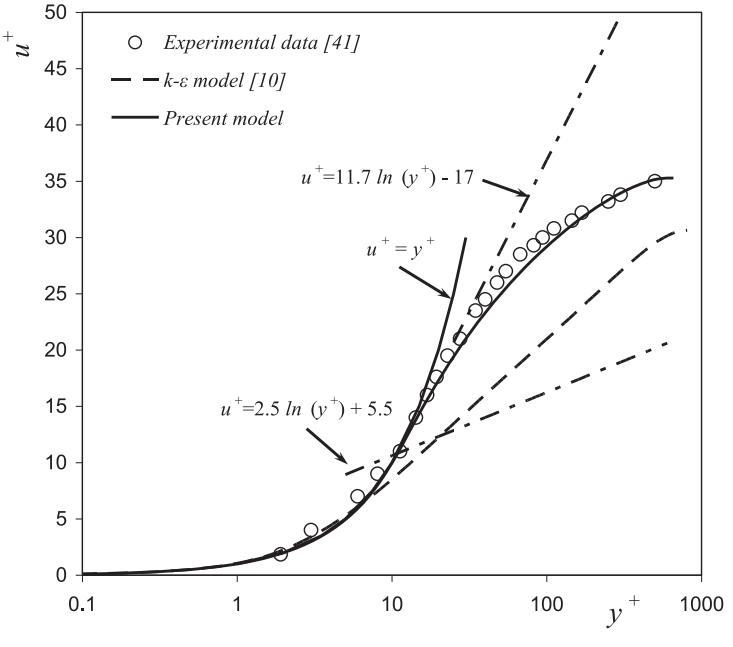

Figure 16. Comparison between the predicted and measured mean velocity profile for fully developed turbulent pipe flow with the 0.2% XG solution at Re = 39,000 in wall coordinates.

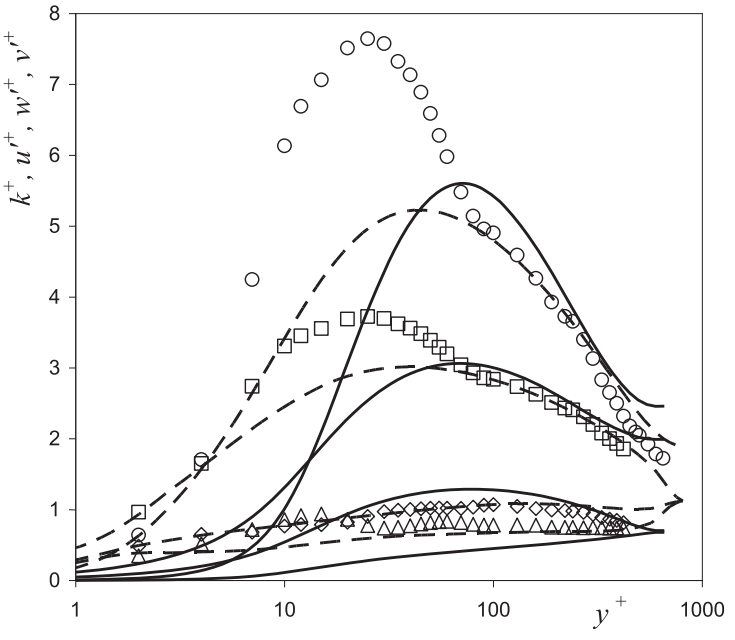

Figure 17. Comparison between the predicted (lines) and the measured (symbols) profiles of normalised turbulent kinetic energy and Reynolds normal stresses for fully developed turbulent pipe flow of 0.20% XG fluid at Re = 39,000 in wall coordinates: ○ k^+ data [41]; □ u'^+, ◊ w'^+, Δ v'^+ data [10]; — present model; - - k–ε model [10].

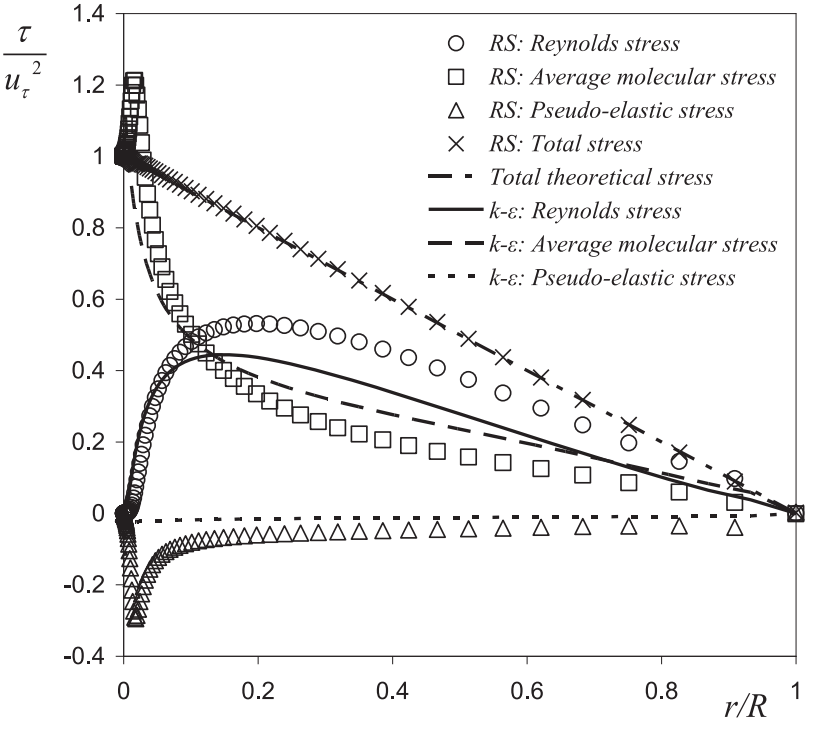

Figure 18. Comparison between the Reynolds stress and k–ε turbulence models of the various shear stresses across the pipe for 0.2% XG at Re = 39,000.

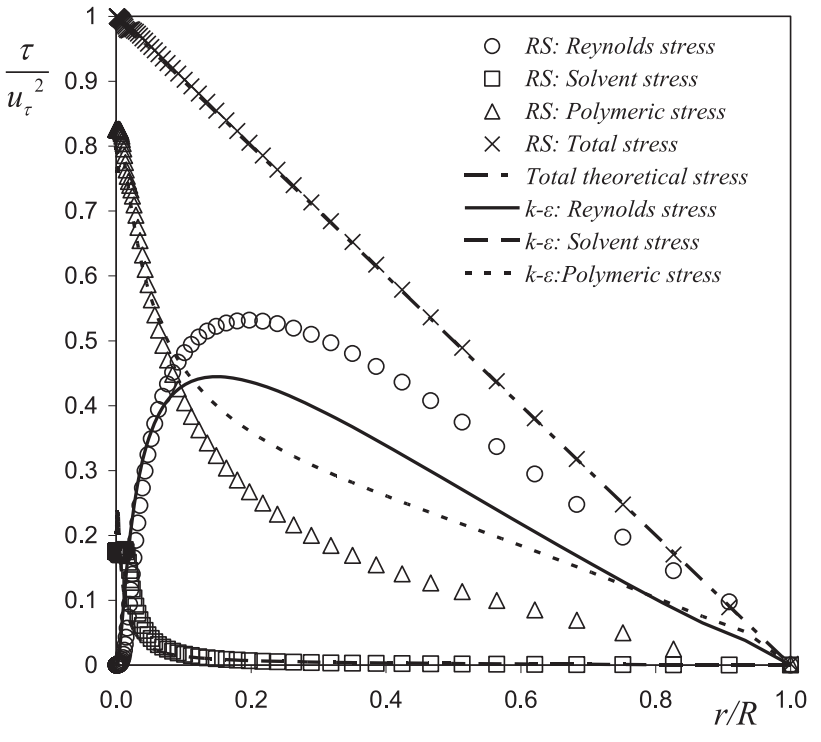

Figure 19. Distributions of the various shear stresses predictions by the Reynolds stress (RS) and k–ε turbulent models, across the pipe for 0.2% XG at Re = 39,000.

6.1. *Comparison with turbulence models for FENE-P fluids*

As referred to at the introduction, there have been recent developments in turbulence modelling for fluids described by the FENE-P constitutive equation and these developments are grounded on DNS results. However, as was also referred to, the DNS predictions with a given set of FENE-P models fitted to real fluids do not match quantitatively the corresponding experimental observations, as described in detail in Ptasinski et al. [14].

Nevertheless, we compare predictions by the present turbulence model with both experimental and DNS data-sets of Ptasinski et al. [14]. In order to do so, we must first quantify the rheological parameters, and for this reason we fit the modified GNF model to the rheology of the FENE-P fluid of [14] for different runs (e.g., their Run A with $L = 10$, $\beta = 0.6$, $\mathrm{We}_{\tau_0} = 54$, $\mathrm{Re}_w = 8609$ and $\eta_w/\eta_0 = 0.792$). The shear and extensional viscosities of the FENE-P model are given by Purnode and Crochet [48]. Figure 20 (a) and (b) plots the shear viscosity and the Trouton ratio, respectively, for both the GNF and FENE-P models. Here the fit of the GNF model to determine n and $K_v$was only in the region of the measured data. The extensional viscosity is related to the Trouton ratio through the relation: $\mathrm{Tr} = \eta_e(\dot{\varepsilon})/3\eta_v(\dot{\gamma})$. As is obvious from Figure 20 (b), the FENE-P predicts two plateaux with an abrupt variation in the middle, whereas the GNF model cannot predict the plateaux, so a simple power law was fit to the range of shear rates from 10^{-4} to 10^{+5} s^{-1}, as in the plot, giving the coefficients p and K_e (details on the coefficients can be found in [8]). Figure 20 also includes data for two cases at $\mathrm{Re}_{\tau_0} = 1000$ as discussed below.

Figure 21 compares the velocity profiles in turbulent channel flow predicted by our RS model, with the GNF model adjusted as in Figure 20 (a) and 20 (b), with the experiments

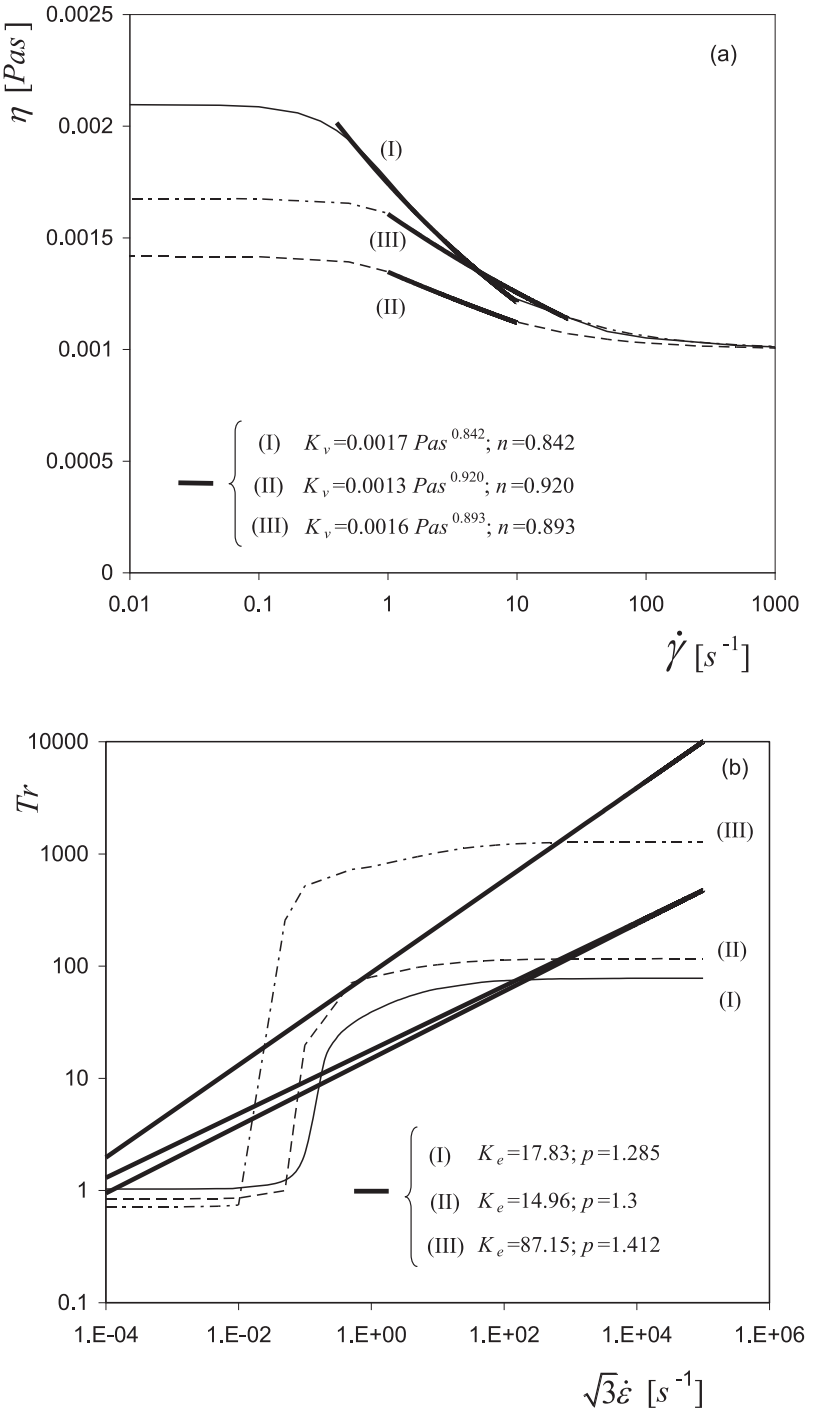

Figure 20. Comparison between the steady viscosities for the FENE-P model of [14,50] equivalent to case A (I), and [49–51] for the run DR = 30%, Thais1 (II) and DR = 58%, Thais2 (III), and the modified GNF model: (a) shear viscosity; (b) Trouton ratio.

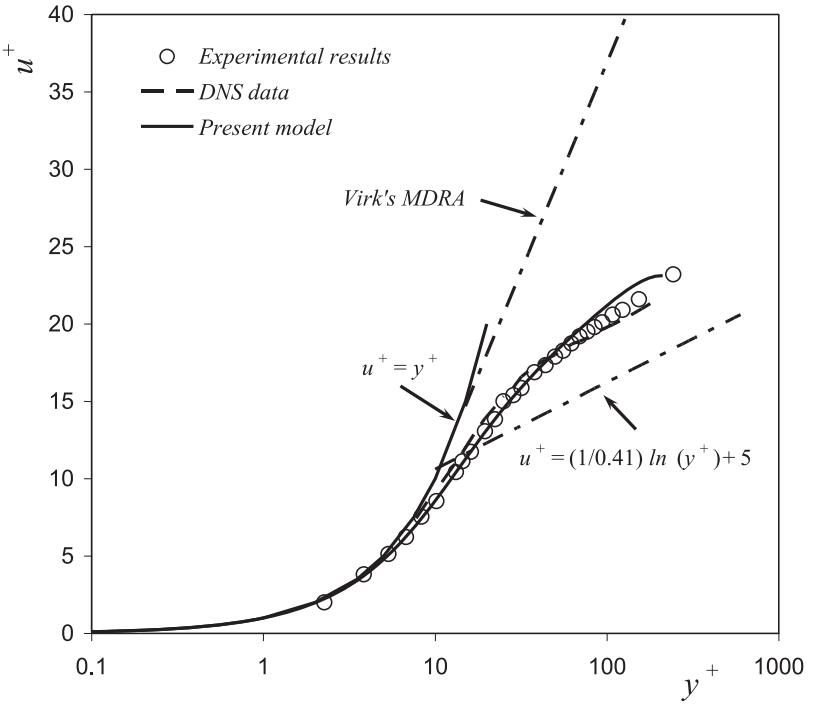

Figure 21. Comparison between the Reynolds stress model predictions (line), DNS data (dashed line) and experimental data (symbols) of [14,50].

and DNS data of Ptasinski et al. [14] (their Exp A which is equivalent to their DNS Run A), which we call here Case A. The predictions by the RS model compare well with the experimental data. In addition, Table 5 compares the drag reduction of the experimental and DNS data of Ptasinski et al. [14] with the simulations of this RS model for Case A. Although the RS predictions compare well with the measured velocity profile, there is an over-prediction of the amount of DR. Similarly, if we compare the experimental data of Ptasinski et al. [14] with the DNS data of Li et al. [11] equivalent to DR = 29%, we observe that both velocity profiles coincide, but we obtain different drag reductions, DR = 29% against DR = 23% of [14].

To understand better, the RS model limitations of other cases were simulated based on the FENE-P model data of Ptasinski et al. [14] such as their Run D, which pertains to the intermediate DR region. As listed in Table 5, in this case, the DR of the RS prediction is

Table 5. Comparison between the drag reductions of the experiments and DNS simulations of Ptasinski et al. [14] and the prediction of this RANS model.

Description	[14] (experimental)	[14] (DNS)	Reynolds stress model
DR	23% (Exp A)	26% (Run A)	32% (Case A)
	–	40% (Run D)	39% (Case D)
	63% (Exp B)	61% (Run B)	– (Case B)

Note: For the DNS data, the FENE-P model coefficients are not from experiments but modified by Ptasinski et al. [14] to provide the correct drag reduction.

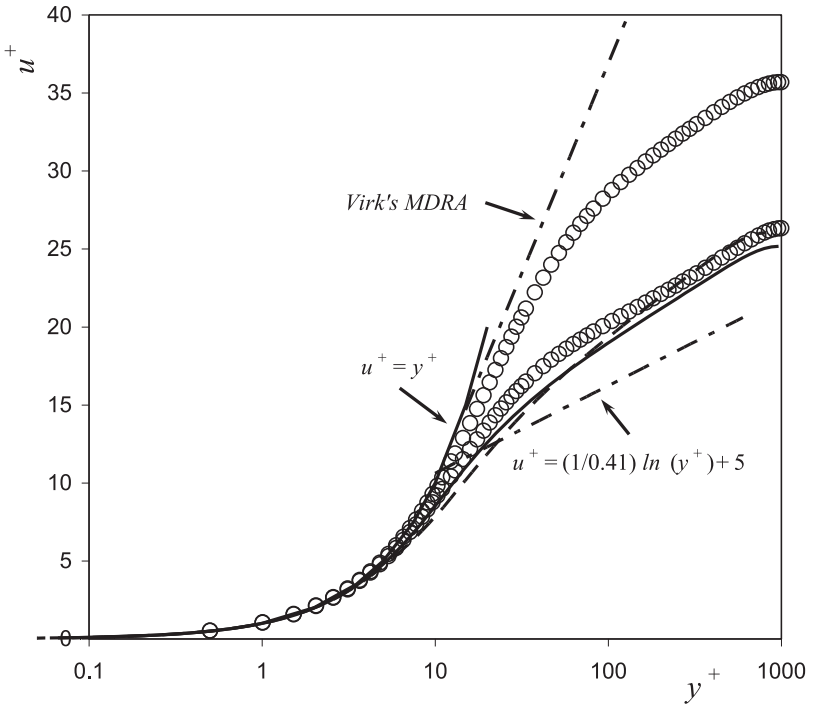

Figure 22. Comparison between the Reynolds stress model predictions (line) and DNS data (symbols) of [49–51]: ○ DNS data; — present model (equivalent to DR = 30%, Thais1); - - present model (equivalent to DR = 58%, Thais2).

nearly the same as for the DNS simulation. For Case B pertaining to high drag reduction, we could not obtain converged solutions with our model and code, because the corresponding flow Reynolds number was too small, within the transition regime.

Finally, to assess the behaviour of the RS model against high Reynolds number DNS of FENE-P fluids, comparisons also carried out against data of Thais et al. [49–51]. We adjusted the rheological parameters of the GNF constitutive equation to represent the FENE-P for the following two cases: flow case Thais1 (DR = 30%, $\mathrm{We}_{\tau_0} = 50$, $\mathrm{Re}_{\tau_0} = 1000$, $L = 30$ and $\beta = 0.9$) and flow case Thais2 (DR = 58%, $\mathrm{We}_{\tau_0} = 115$, $\mathrm{Re}_{\tau_0} = 1000$, $L = 100$ and $\beta = 0.9$) and the corresponding plots of the steady shear and extensional viscosities appear in Figure 20. Figure 22 compares the predicted mean velocity profiles with the corresponding DNS data. For the $\mathrm{Re}_{\tau_0} = 1000$, DR = 30% flow (Thais1), the model underpredicts the velocity profile, which corresponds to a predicted DR = 23%. Increasing the Weissenberg number to that of the Thais2 flow conditions, DR = 58%, and above, convergence difficulties arise due to excessive turbulence dampening by the model first in the buffer layer and at higher Weissenberg numbers in the log-law region. For the Thais2 case, the model still converges but provides unrealistic results, shown by the thick dashed velocity profile of Figure 22, which is close to that of the DR = 30% case, but exhibits lower velocities in the buffer layer. The corresponding profile of the turbulent kinetic energy (not shown for conciseness) shows excessive turbulence dampening in the buffer layer.

This is due to the very high values of the properties K_e and p quantifying the dimensionless strain-hardening extensional viscosity (η_e^* in Equation (4)) and their unbounded nature (near the wall this quantity can be very high, unless it is controlled by the

dampening function f_v). This result for the Thais2 flow case is in line with previous observations of convergence difficulties for fluids with very high drag reductions (DR > 60%) when associated with very high values of K_e and p as was the case for a solution of 0.2% PAA [8] for which we could never obtain converged predictions with this class of turbulence closures. This problem is independent of the Reynolds number except in regard to a possible reduction of the dampening effect of $f_v$with increasing Re but there is no clear value of K_e and p establishing the limit of application of the model since it also depends on other quantities, like K_v and n. Nevertheless, an excessive decrease of u^+ in the buffer layer region accompanied by a severe reduction of turbulence indicates that the upper limit of the model has been reached.

These comparisons with DNS data of FENE-P model should always be looked upon with some caution. After all, the current class of turbulence models were developed exclusively on the basis of experimental data, including data from the opposed jet rheometer for the extensional viscosity. Simultaneously, we stress again that none of the DNS data-sets for FENE-P in the literature has ever been matched quantitatively with experimental data both in terms of rheology and fluid dynamics.

7. Conclusions

An RS model has been developed to predict the flow of viscoelastic solutions based on a generalised Newtonian constitutive equation modified to account for elastic effects. The RS model is a modified version of the low Reynolds number turbulence model of Lai and So [35] and includes several new non-Newtonian terms. Closures for all these new terms were developed as well as for the pseudo-elastic stress term appearing in the momentum equation to better describe turbulence anisotropy so common in turbulent flows of viscoelastic fluids.

The predictions of friction factor and mean velocity profiles by this model are good for all fluids tested. In particular, this turbulence model was able to successfully predict the flows involving polymer solutions containing the semi-rigid XG molecule, for which the linear and nonlinear $k-\varepsilon$ models of [9,10] systematically underpredicted the measured levels of drag reduction. Regarding turbulence quantities, the model was able to capture the enhanced turbulence anisotropy with drag reduction and the shift away from the wall of the peak values of k typical of increasing drag reduction levels. However, the streamwise Reynolds normal stress ($\overline{u^2}$) was, in general, underpredicted especially near the wall. The tangential normal RS ($\overline{w^2}$) was always well predicted, and in all cases $\overline{v^2}$ was underpredicted, near and away from the wall. Note that these predictions of the normal stresses are as good as those obtained by the anisotropic $k-\varepsilon$ model of Resende et al. [10].

We also analysed the performance of the present model against experimental data for channel flow from the literature and the corresponding set of DNS simulations, which were based on the FENE-P rheological constitutive equation. The DNS data-sets predicted well the measured DR only because the FENE-P coefficients, and in particular the model relaxation time, were adjusted for that purpose, not adjusted to the experimentally measured relaxation time. Our GNF model, which was adjusted to the fluid shear rheology and to the FENE-P Trouton ratio, also provided good predictions, even though not as good as those of the DNS. This RS model behaves well at low and intermediate DR but can become unstable close to the maximum DR, especially when the flow Reynolds number is low and close to the transition regime if the values of K_e and p are very high.

Even though the present model represents a significant improvement over the previous turbulence models for viscoelastic solutions, all of which are two-equation models, it will be necessary to extend the analysis to more complex geometries in order to assess whether

the RS model is able to behave effectively. Since the changes to the original model of Lai and So were kept to a minimum, it is our belief that this model will perform better than the earlier two-equation closures of [9,10].

Acknowledgements

The authors would like to acknowledge funding of FEDER via grants POCI/56342/EQU/2004 and POCI/59338/EME/2004 of Fundação para a Ciência e Tecnologia (FCT). P.R. Resende wishes also to acknowledge FCT for personal funding via SFRH/BD/18475/2004.

References

[1] T. Mizushina, H. Usui, and T. Yoshida, *Turbulent pipe flow of dilute polymer solutions*, J. Chem. Eng. Jpn. 7 (1973), pp. 162–167.
[2] F. Durst and A.K. Rastogi, *Calculations of turbulent boundary layer flows with drag reducing polymer additives*, Phys. Fluids 20 (1977), pp. 1975–1985.
[3] S. Hassid and M. Poreh, *A turbulent energy dissipation model for flows with drag reduction*, J. Fluids Eng. 100 (1978), pp. 107–112.
[4] S. Politis, *Turbulence modelling on inelastic power-law fluids*, Internal report 52, BRITE project RIIB.0085.UK, Imperial College of Science, Technology and Medicine, London, UK, 1989.
[5] M.R. Malin, *Turbulent pipe flow of power-law fluids*, Int. Commun. Heat Mass Transfer 24 (1997), pp. 977–988.
[6] D.O.A. Cruz, C.E. Maneschy, and E.N. Macedo, *A turbulence model for computing the flow of power law fluids within circular tubes*, Hybrid Methods Eng. 2 (2000), pp. 1–13.
[7] F.T. Pinho, *A GNF framework for turbulent flow models of drag reducing fluids and proposal for a k-ε type closure*. J. Non-Newton Fluid Mech. 114 (2003), pp. 149–184.
[8] D.O.A. Cruz and F.T. Pinho, *Turbulent pipe flow predictions with a low Reynolds number k-ε model for drag reducing fluids*, J. Non-Newton Fluid Mech. 114 (2003), pp. 109–148.
[9] D.O.A. Cruz, F.T. Pinho, and P.R. Resende, *Modeling the new stress for improved drag reduction predictions of viscoelastic pipe flow*, J. Non-Newton Fluid Mech. 121 (2004), pp. 127–141.
[10] P.R. Resende, M.P. Escudier, F. Presti, F.T. Pinho, and D.O.A. Cruz, *Numerical predictions and measurements of Reynolds normal stresses in turbulent pipe flow of polymers*, Int. J. Heat Fluid Flow 27 (2006), pp. 204–219.
[11] C.F. Li, R. Sureshkumar, and B. Khomami, *Influence of rheological parameters on polymer induced turbulent drag reduction*, J. Non-Newton Fluid Mech. 140 (2006), pp. 23–40.
[12] C.D. Dimitropoulos, R. Sureshkumar, and A.N. Beris, *Direct numeric simulation of viscoelastic turbulent channel flow exhibiting drag reduction: Effect of variation of rheological parameters*, J. Non-Newton Fluid Mech. 79 (1998), pp. 433–468.
[13] B. Yu and Y. Kawaguchi, *Effect of Weissenberg number on the flow structure: DNS study of drag reducing flow with surfactant additives*, Int. J. Heat Fluid Flow 24 (2003), pp. 491–499.
[14] P.K. Ptasinski, B.J. Boersma, F.T.M. Nieuwstadt, M.A. Hulsen, B.H.A.A. Van Den Brule, and J.C.R. Hunt, *Turbulent channel flow near maximum drag reduction: Simulation, experiments and mechanisms*. J. Fluid Mech. 490 (2003), pp. 251–291.
[15] G. Lielens, R. Keunings, and V. Legat, *The FENE-L and FENE-LS closure approximations to the kinetic theory of finitely extensible dumbbells*, J. Non-Newton Fluid Mech. 87 (1999), pp. 179–196.
[16] Q. Zhou and R. Akhavan, *A comparison of FENE and FENE-P dumbbell and chain models in turbulent flow*, J. Non-Newton Fluid Mech. 109 (2003), pp. 115–155.
[17] C.F. Li, V.K. Gupta, R. Sureshkmar, and B. Khomami, *Turbulent channel flow of dilute polymeric solutions: Drag reduction scaling and an eddy viscosity model*, J. Non-Newton Fluid Mech. 139 (2006), pp. 177–189.
[18] F.T. Pinho, C.F. Li, B.A. Younis, and R. Sureshkumar, *A low Reynolds number k-ε turbulence model for FENE-P viscoelastic fluids*, J. Non-Newton Fluid Mech. 154 (2008), pp. 89–108.
[19] P.R. Resende, K. Kim, B.A. Younis, R. Sureshkumar, and F.T. Pinho, *A k-ε turbulence model for FENE-P fluid flows at low and intermediate regimes of polymer-induced drag reduction*, J. Non-Newton Fluid Mech. 166 (2011), pp. 639–660.

[20] P.R. Resende, F.T. Pinho, B.A. Younis, K. Kim, and R. Sureshkumar, *Development of a low-Reynolds-number k-ω model for FENE-P fluids*, Flow Turbul. Combust. 90 (2013), pp. 69–94.

[21] Y. Dubief, G. Laccarino, and S.K. Lele, *A turbulence model for polymer flows*, Int. Rep., Annual Research Brief, Center for Turbulence Research, Stanford, CA, 2004.

[22] G. Iaccarino, E.S.G. Shaqfeh, and Y. Dubief, *Reynolds-averaged modeling of polymer drag reduction in turbulent flows*, J.Non-Newton Fluid Mech. 165 (2010), pp. 376–384.

[23] P.A. Durbin, *Application of a near-wall turbulence model to boundary layers and heat transfer*, Int. J. Heat Fluid Flow 14 (1993), pp. 316–323.

[24] Y. Nagano and M. Hishida, *Improved form of the k-ε model for wall turbulent shear flows*, J. Fluids Eng. 109 (1987), pp. 156–160.

[25] P.K. Ptasinski, F.T.M. Nieuwstadt, B.H.A.A. Van Den Brule, and M.A. Hulsen, *Experiments in turbulent pipe flow with polymer additives at maximum drag reduction*, Flow Turbul. Combust. 66 (2001), pp. 159–182.

[26] K.D. Housiadas and A.N. Beris, *Polymer-induced drag reduction: Effects of the variations in elasticity and inertia in turbulent viscoelastic channel flow*, Phys. Fluids 15 (2003), pp. 2369–2384.

[27] V.C. Patel, W. Rodi, and G. Scheuerer, *Turbulence models for near-wall and low Reynolds: A review*, AIAA J. 23 (1984), pp. 1308–1319.

[28] T.S. Park, H.J. Sung, and K. Suzuki, *Development of a nonlinear near-wall turbulence model for turbulent flow and heat transfer*, Int. J. Heat Fluid Flow 24 (2003), pp. 29–40.

[29] T.J. Craft, B.E. Launder, and K. Suga, *Development and application of a cubic eddy-viscosity model of turbulence*, Int. J. Heat Fluid Flow 17 (1996), pp. 108–115.

[30] B.E. Launder, G.J. Reece, and W. Rodi, *Progress in the development of a Reynolds-stress turbulence closure*, J. Fluid Mech. 68 (1975), pp. 537–566.

[31] K. Hanjalic and B.E. Launder, *Contribution towards a Reynolds-stress closure for low-Reynolds-number turbulence*, J. Fluid Mech. 74 (1976), pp. 593–610.

[32] B.E. Launder and W.C. Reynolds, *Asymptotic near-wall stress dissipation rates in a turbulent flow*, Phys. Fluids 26 (1983), pp. 1157–1158.

[33] M. Prud'homme and S. Elghobashi, *Turbulent heat transfer near the reattachment of flow downstream of a sudden pipe expansion*, Numer. Heat Transfer 10 (1986), pp. 349–368.

[34] R.M.C. So and G.J. Yoo, *Low-Reynolds-number modelling of turbulent flows with and without wall transpiration*, AIAA J. 25 (1987), pp. 1556–1564.

[35] Y.G. Lai and R.M.C. So, *On near-wall turbulent flow modelling*, J. Fluid Mech. 221 (1990), pp. 641–673.

[36] N. Shima, *A Reynolds-stress model for near-wall and low Reynolds-number regions*, J. Fluids Eng. 110 (1988), pp. 38–44.

[37] S.S. Thakre and J.B. Joshi, *A low Reynolds number Reynolds stress modelling of turbulent pipe flow: Flow pattern and energy balance*, Chem. Eng. Commun. 189 (2002), pp. 759–785.

[38] T.J. Craft, *Developments in a low-Reynolds-number second-moment closure and its application to separating and reattaching flows*, Int. J. Heat Fluid Flow 19 (1998), pp. 541–548.

[39] T.J. Craft, and B.E. Launder, *A Reynolds stress closure designed for complex geometries*, Int. J. Heat Fluid Flow 17 (1996), pp. 245–254.

[40] N. Shima, *Low-Reynolds-number second-moment closure without wall-reflection redistribution terms*, Int. J. Heat Fluid Flow 19 (1998), pp. 549–555.

[41] M.P. Escudier, F. Presti, and S. Smith, *Drag reduction in the turbulent pipe flow of polymers*, J. Non-Newton Fluid Mech. 81 (1999), pp. 197–213.

[42] H.A. Barnes, J.F. Hutton, and K. Walters, *An Introduction to Rheology*, Elsevier, Amsterdam, 1989.

[43] C.D. Dimitropoulos, R. Sureshkumar, A.N. Beris, and R.A. Handler, *Budgets of Reynolds stress, kinetic energy and streamwise entropy in viscoelastic turbulent channel flow*, Phys. Fluids 13 (2001), pp. 1016–1027.

[44] J. Laufer, *The structure of turbulence in fully developed pipe flow*, NACA Rep. 1174, National Advisory Committee for Aeronautics, Washington, 1954.

[45] E.R. Van Driest, *On turbulent flow near a wall*, J. Aeronautical Sci. 23 (1956), pp. 1007–1011.

[46] F. Durst, J. Jovanovic, and J. Sender, *LDA measurements in the near-wall region of turbulent pipe flow*, J. Fluid Mech. 295 (1995), pp. 305–335.

[47] P.S. Virk, H.S. Micley and K.A. Smith, *The ultimate asymptote and mean flow structure in Tom's phenomenon*, J. Appl. Mech. 92 (1970), pp. 488–493.

[48] B. Purnode and M.J. Crochet, *Polymer solution characterization with the FENE-P model*, J. Non-Newton Fluid Mech. 77 (1998), pp. 1–20.
[49] L. Thais, G. Mompean, and T.B. Gatski, *Spectral analysis of turbulent viscoelastic and Newtonian channel flows*, J. Non-Newton Fluid Mech. 200 (2013), pp. 165–176.
[50] L. Thais, A.E. Tejada-Martínez, T.B. Gatski, and G. Mompean, *Temporal large eddy simulations of turbulent viscoelastic drag reduction flows*, Phys. Fluids 22 (2010), pp. 1–13.
[51] L. Thais, T.B. Gatski, and G. Mompean, *Analysis of polymer drag reduction mechanisms from energy budgets*, Int. J. Heat Fluid Flow 43 (2013), pp. 52–61.